POSITIVE AND NEGATIVE PION ELASTIC SCATTERING ON ^{58}Ni,^{60}Ni, AND ^{64}Ni AT 50 MEV AND 65 MEV

by

Brian Edwin Fick

Dissertation submitted to the Faculty of the

Virginia Polytechnic Institute and State University

in partial fulfillment of the requirements for the degree of

DOCTOR OF PHILOSOPHY

in

Physics

APPROVED:

M. Blecher, Chairman

R. A. Arndt

J. R. Ficenec

K. Gotow

T. Mizutani

June, 1985

Blacksburg, Virginia

POSITIVE AND NEGATIVE PION ELASTIC SCATTERING ON ^{58}Ni,^{60}Ni, AND ^{64}Ni AT 50 MEV AND 65 MEV

by

Brian Edwin Fick

(ABSTRACT)

Elastic scattering data was successfully taken using the new "Clamshell" spectrometer. Angular distributions of elastic differential cross sections were obtained at 50 MeV and 65 MeV using positive and negative pions scattered from ^{58}Ni, ^{60}Ni, and ^{64}Ni.

The data were compared to predictions made using the MSU optical potential. The π^+ data agreed fairly well with the predictions at both 50 MeV and 65 MeV while the corresponding π^- data significantly disagreed with the predictions.

The absorption parameters in the MSU potential were varied in an attempt to fit the data. A suitable fit was achieved for both π^+ and π^- data at 50 MeV and 65 MeV. The real part of the p–wave absorption parameter was well determined but showed two distinct values for π^+ and π^- indicating that there is a seperate potential for π^+ and π^- or that the absorption part of the potential is inadequately formulated.

ACKNOWLEDGEMENTS

I would like to gratefully acknowledge my advisors Marvin Blecher and Kazuo Gotow for providing me with a fine dissertation project and the generous means with which to pursue it. Their model as experimentalists was truly inspirational to me. I would also like to personally thank Dennis Wright for his valuable help and advice at every stage of the project.

Thanks go to all the members of experiment 814. They are : G. Blanpied, J. Escalante, D. Mack, S. Mishra, B. Preedom, B. Ritchie, P. Roos, and C. S. Whisnant. Acknowledgement must also be made of Dick Boudrie for directing the elaborate process by which the Clamshell spectrometer successfully came into being. I would also like to thank for imparting his expertise at chamber making to an amateur like me. I am also grateful to my loving wife for her moral support and tremendous patience with me as I spent almost one third of my time away from home working on the project.

TABLE OF CONTENTS

LIST OF FIGURES

LIST OF FIGURES (cont)

Figure Page

LIST OF TABLES

Table Page

Chapter I

Introduction

Ever since it was realized that pions mediate the long range part of the strong nuclear force scientists have recognized the pion's potential as a probe of nuclear structure. Whereas probes such as electrons, muons and photons accurately search out the charged structure of the nucleus pions react to the uncharged constituents as well as charged via the strong interaction. As nuclear probes protons and neutrons are also sensitive to the strong force but at low energies they have a much shorter mean free path in nuclear matter than do pions. Also, the half integer spin of the nucleon complicates the interaction. The scattering of the spin–0 pion with a nucleus is intrinsically simpler to interpret. In addition, the pion has unique properties which open up new ways of viewing the nucleus. For example, the pion is capable of being absorbed outright by the constituents of the nucleus. Also the fact that the pion comes as a charge triplet π^+, π^0 and π^- allows for the possibility of not only single charge exchange as in nucleon scattering but double charge exchange reactions as well.

It is of interest to anyone trying to explore the nucleus with pions to try to first understand the pion–nucleus interaction mechanism. The most obvious path toward this goal is to try to use the simpler two particle π–nucleon interaction to build a solution to the problem of the interaction of the pion with the entire complex target. One is forced to use a many–body treatment because it is known that some observed scattering phenomena require more than one

nuclear constituent to be involved in a given interaction. An example of this is the case of true pion absorption, $\pi + N \rightarrow N$ which can only take place in the presence of other particles in order that the balance of energy and momentum is preserved. Usually this occurs on a pair of nucleons. Another case is the effect which the Pauli principle plays in blocking some interactions because of the presence of more than one fermion in the nucleus.

The many–body nature of the scattering problem is reminiscent of the situation in optics where the effects of all the scatterings from the myriad of atoms in a substance are combined into the index of refraction. Thus, by analogy to what is done in optics the nucleus with its many scatterers is approximated by a single complex potential called an optical potential. This potential is independent of the coordinates of the individiual nucleons and depends only on the coordinates of the pion with respect to the nucleus as a whole. The complex part of the potential takes into account everything which is lost from the elastic channel. In particular, this applies to inelastic collisions, charge exchange reactions, reactions in which intermediate excited states of the pion or nucleons exist etc. The real part describes elastic scattering.

The optical potential U_{opt} can be related to the pion–nucleus scattering amplitude, T_N, by the following expression [1]:

$$T_N = U_{opt} + U_{opt}a^{-1}T_N$$

$$= \Sigma t_i + \Sigma t_i a^{-1} T_N$$

$$a^{-1} \equiv E_a - H_0 + i\varepsilon$$

Where $H_0 = H_N + h$; H_N being the nuclear Hamiltonian, h the kinetic energy

operator and E_a the total energy. ε is inserted to prevent a^{-1} from blowing up when H_0 operates on one of its eigenfunctions. t_i is the interaction amplitude between the pion and the i'th bound nucleon. In the impulse approximation t_i is replaced by the corresponding amplitude for an unbound nucleon. The pion–nucleus scattering amplitude and consequently the optical potential can be built up from this expression recursively via a multiple scattering series [2]. The MSU potential [3], the potential which will be used to analyze the data in this thesis, was constructed in this manner.

There are several advantages to doing π–nucleus scattering experiments at low energies. At energies above about 100 MeV the π–N total cross section begins to exhibit a series of bumps or resonances as can be seen in the π–p cross sections in figure I–1. The first such resonance occurs at 180 MeV. If the cross section is split up into s–wave and p–wave parts, it is found that this resonance is only visible in the p–wave part. Thus, when doing pion–nucleon scattering at energies approaching the resonance energy the interaction becomes much stronger and this strength is added to the angular momentum=1 or p–wave part of the interaction. Below resonance energies the π–p interaction quickly weakens. This weaker single particle interaction facilitates the use of the multiple scattering series mentioned above. Another effect of the weakening is to increase the depth in the nucleus to which the pion can penetrate before interacting. This is possible because the mean free path in the nuclear medium goes roughly as the inverse of the total cross section and the nuclear density. The result of this relative transparency of the nucleus to pions is to make low

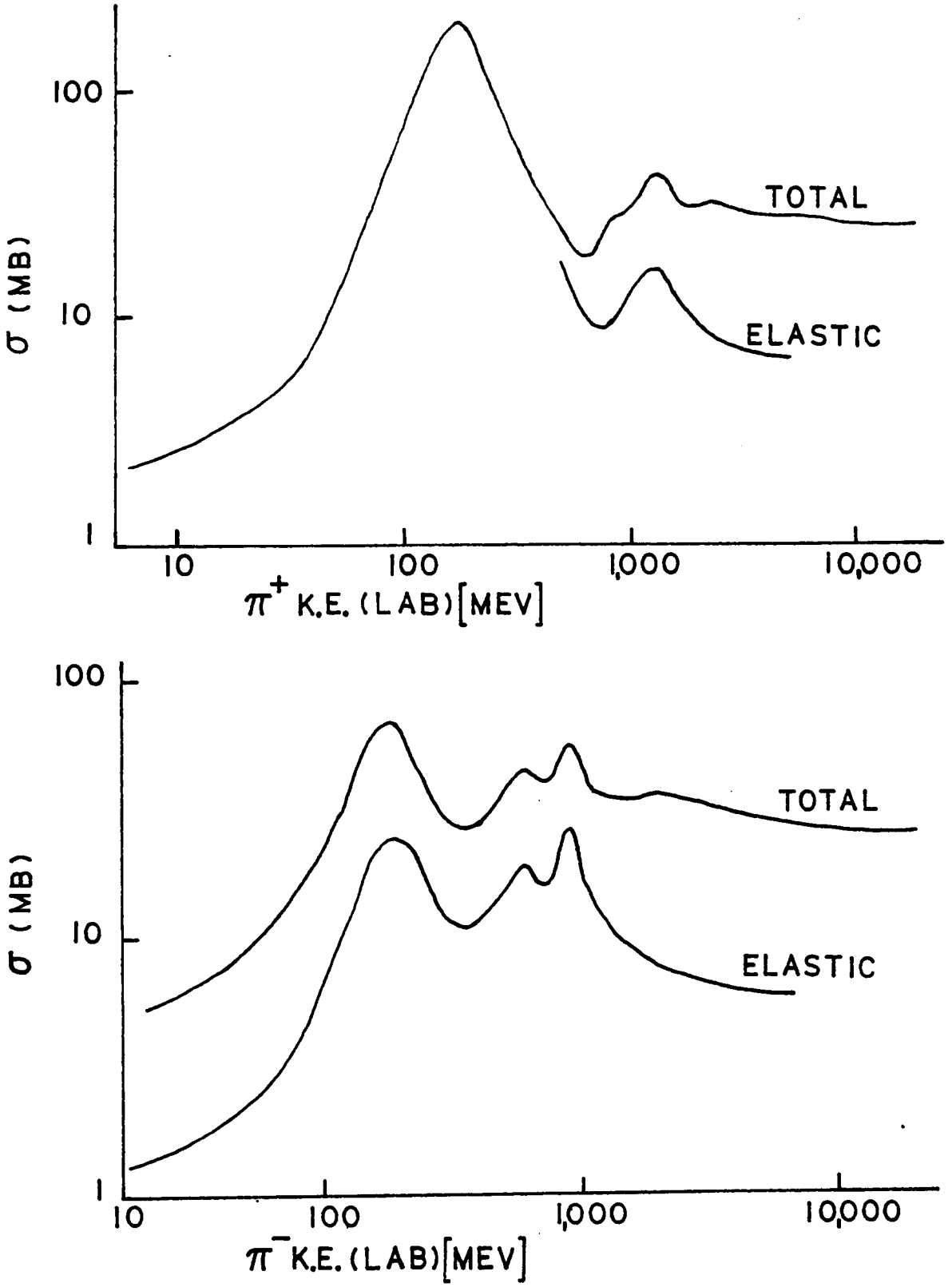

Figure I-1 Pion-proton cross sections vs. pion kinetic energy

energy phenomena richer and theoretical treatment correspondingly more complicated. At resonance energies the theories are simpler and more successful at explaining behavior because only phenomena at the very surface of the nucleus affect the nature of the cross sections.

The task of this thesis is threefold. First, a new spectrometer system and the first experiment for which it has been used will be described. Second, a comparison between the resulting data and optical model predictions will be made. Third, further optical model analyses will be undertaken to explore the validity of the MSU optical potential at an energy of 65 MeV, which is above the usual energy range of this potential. Chapter II describes the experiment and apparatus, chapter III explains the process of taking raw data and producing useable cross sections, chapter IV presents and comments on the data and then analyzes it using optical potentials, and chapter V presents a brief summary of the results.

Chapter II

The Experiment

A. Experimental Procedure

The experiment was performed using the new "Clamshell" spectrometer at the Los Alamos Meson Physics Facility (LAMPF) between July 4 and July 15, 1984. The experiment was preceded by a two week long development period in which the spectrometer system was assembled and tested. Specifically, the experiment consisted of elastically scattering positive and negative pions from ^{58}Ni, ^{60}Ni and ^{64}Ni. Nickle was chosen as a target because it has three easily obtainable isotopes, each having a first excited state which is more than one MeV removed from the ground state. The targets were all self-supporting foils of thickness 0.147, 0.151 and 0.146 grams/cm^2, respectively. The incident pion kinetic energies selected were 50 and 65 MeV. The 65 MeV data was obtained for scattering angles of 30, 40, 50, 60, 70, 80, 85, 90, 95, 100 and 110 degrees using both positive and negative pions. The 50 MeV data was obtained only for negative pions at a few strategic scattering angles which were chosen to supplement previous work [4]. Also, because of time constraints only ^{58}Ni and ^{64}Ni targets were employed at 50 MeV.

B. The LEP Channel and Clamshell Spectrometer

The Clamshell spectrometer was positioned at the output of the Low-Energy Pion (LEP) channel [5] at LAMPF (See Fig. II-1). This channel provides high-resolution, variable energy pion beams of 20 to 300 MeV with fluxes up to $1.2 \times 10^{+7}$ π^+/sec. Pions are produced in a rotating wheel target by 800 MeV protons from the LAMPF side-coupled resonant-cavity linac. The entrance of the LEP channel intercepts the pions at a production angle of 45 degrees and presents a maximum solid angle of 17 milli-steradians to the production target. The channel is an achromatic optical system consisting of four bending magnets each of which introduces a 1-meter radius 60-degree bend to the beam in a vertical plane (See Fig. II-2). Focusing quadrupole doublet magnets are positioned at the entrance and the exit of the channel. At the center of the channel proton absorbers were inserted into the beam by remote control to limit proton contamination. The momentum slit at the center of the channel can be remotely varied thus allowing the momentum bite to vary from $\Delta p/p$ = 0.05 % to $\Delta p/p$ = 2.8 %. By varying the fields in the channel magnets it is possible to produce the desired beam profile at the experimental target which is several meters from the output of the channel. For the present experiment it was possible to obtain a target beam spot which was ±1.5 cm. in the horizontal direction and ±0.2 cm. in the vertical direction. The beam divergence at the target was estimated to be ±30 mrad in the vertical and ±90 mrad in the horizontal. The estimates of beam contaminants are 10^{-4}

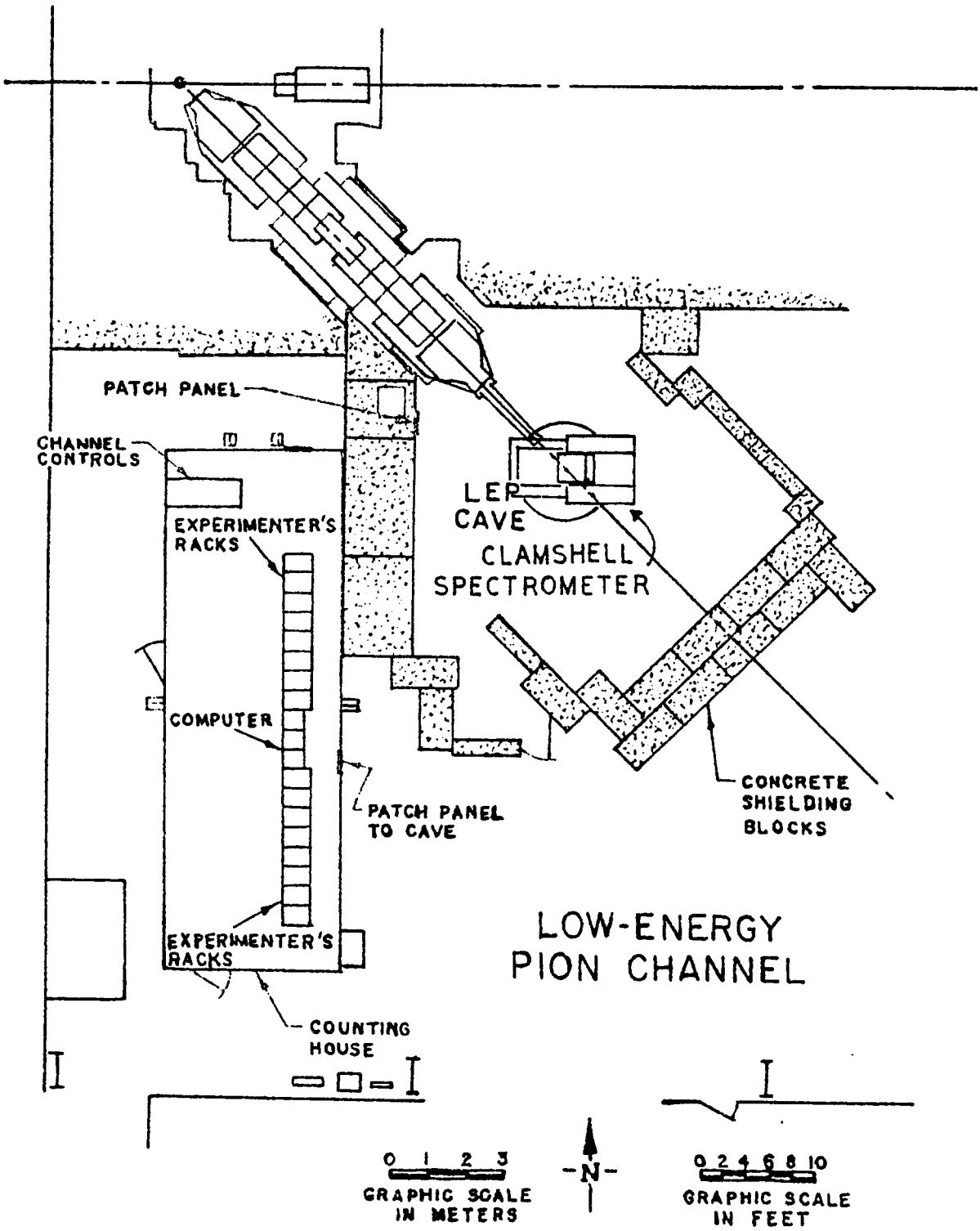

Figure II-1 LEP Channel and Experimental Area

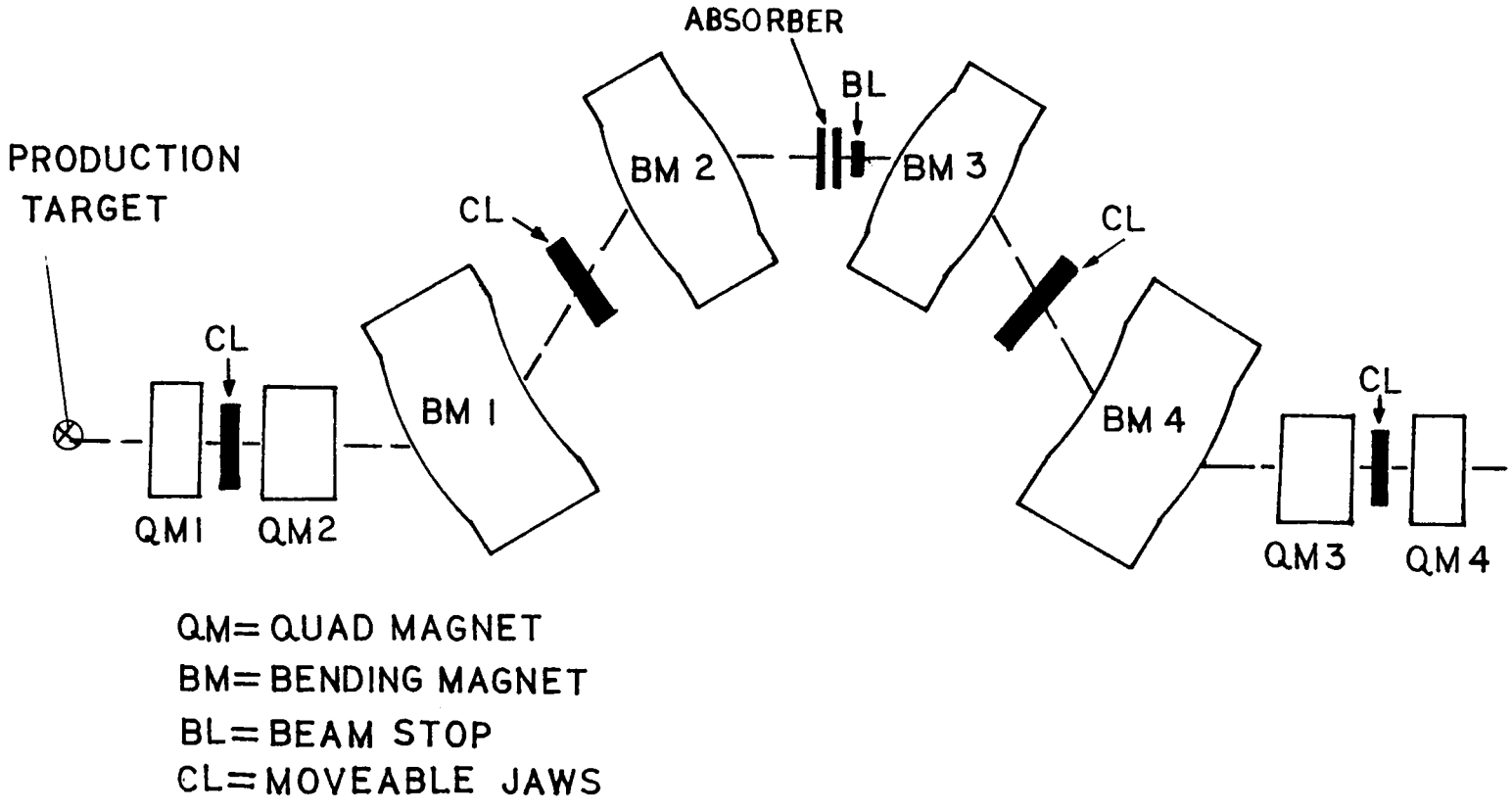

Figure II-2 LAMPF Low Energy Pion Channel.

neutrons/π^+, $10^{-1}\mu$'s/π^+ and 9 x 10^{-1} e^-'s/π^- at 50MeV [6].

The pion beam was monitored [7,8] by using scintillation counter telescopes set to look at decay muons emitted by the beam at the exit of the LEP channel (See Fig. II–3). The telescopes actually observe the $\pi-\mu$ decay phase space jacobian plateau region for a small length of the beam. Each telescope consists of a "near" and a "far" scintillation counter which form a line with the observed region of the beam. The inclination of this line from the beam direction is selected so that the telescope is well within the $\pi-\mu$ decay relativistic opening angle and yet outside of the π beam divergence angle. The label "near" indicates that the given counter is nearer the channel exit whereas the label "far" indicates that the given counter is nearer the experiment target. The number of events coincident between the near and far counters of a given telescope is proportional to the number of pions in the beam. To assess proper alignment of the telescopes the ratio of the number of coincident counts to the number of counts encountered in a small solid angle detector near the production target (BOT) and an upstream toroid detector (Toroid 1) were plotted versus $\Delta p/p$. If the telescopes are really sensitive to the behavior of the beam the plot should indicate a curve which extrapolates to zero for $\Delta p/p=0.0$. Figure II–4 indicates that this was indeed the case.

The experiment was performed with targets in air due to the late delivery of the vacuum scattering chamber. Thus the target holder was simply mounted on a post at the center of rotation of the spectrometer. To reduce multiple scattering due to air a 1–meter long vacuum sealed snout attached to the

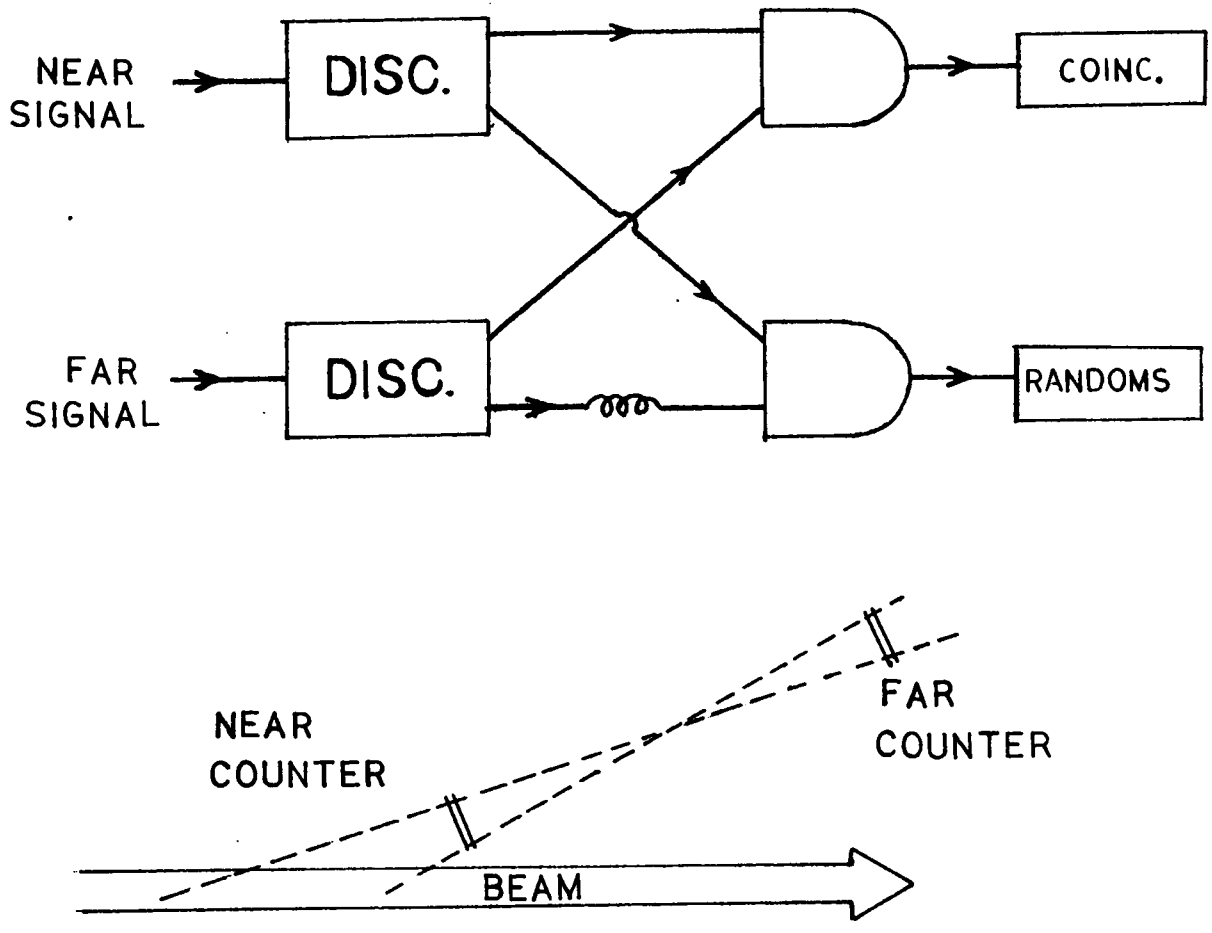

Figure II-3 Beam Monitor Setup and Electronics

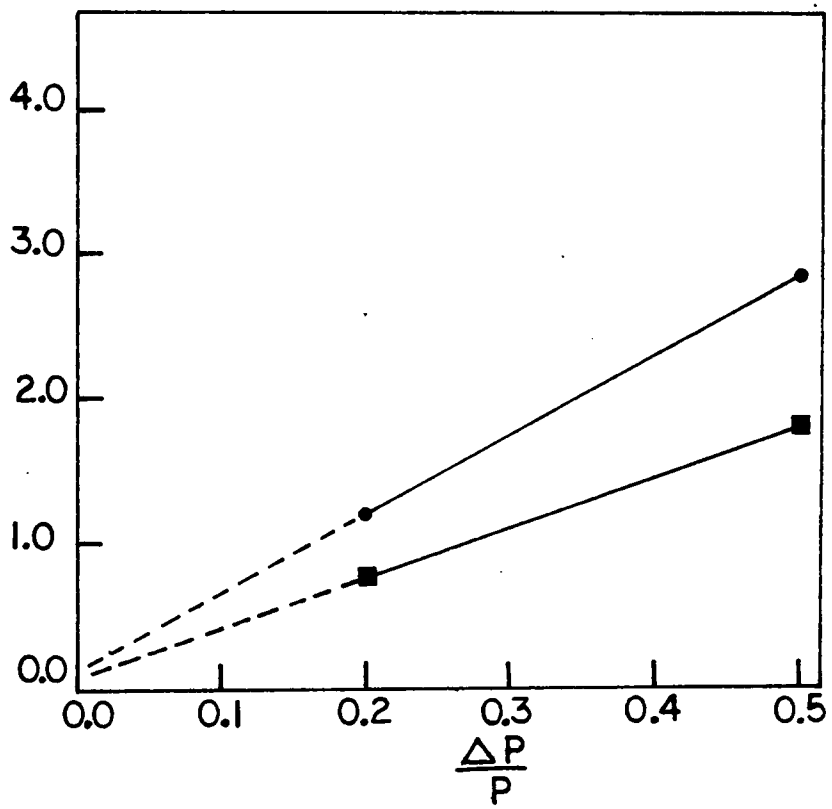

Figure II-4 Ratio of the number of beam monitor counts to • number of BOT counts and ■ number of Toroid 1 counts vs. $\Delta p/p$.

output of the channel and extending to within several centimeters of the target was installed. The scattered particles experience only a few more centmeters of air before they enter the evacuated Clamshell magnet. The spectrometer system setup is shown in figure II–5.

The Clamshell magnet which momentum analyzes the scattering products embodies a novel design [9] which was worked out by Harold Enge and Stanley Kowalski at MIT. It consists simply of a single dipole with a non–uniform field. Its pole faces are planes tilted with respect to each other producing a wedge shaped vacuum gap which varies in width from 10 to 18 centimeters in a direction transverse to the particle trajectories. It is single focusing with a momentum acceptance of ±30 % and a solid angle acceptance of up to 36 milli–steradians. Raytrace calculations indicate that a resolution of 0.1 % can be expected at the center of the focal plane. The relatively short path length of 2 meters aids in minimizing π–decay within the spectrometer.

Positioned at the focal plane of the Clamshell magnet were two drift chamber assemblies which were used to measure the trajectories of charged particles exiting the spectrometer. Each chamber assembly presented a 90 cm by 21 cm active area to the incoming particles. Their long dimension corresponded to the dispersion direction of the magnet. The chamber assemblies were not oriented parallel to the focal plane. They were instead tilted by 20 degrees from it so that the first chamber assembly intersected the focal plane at it's center and rested parallel to the exit window of the magnet's vacuum container. The second chamber assembly, parallel to the first, was 30 cm further along the particle trajectory.

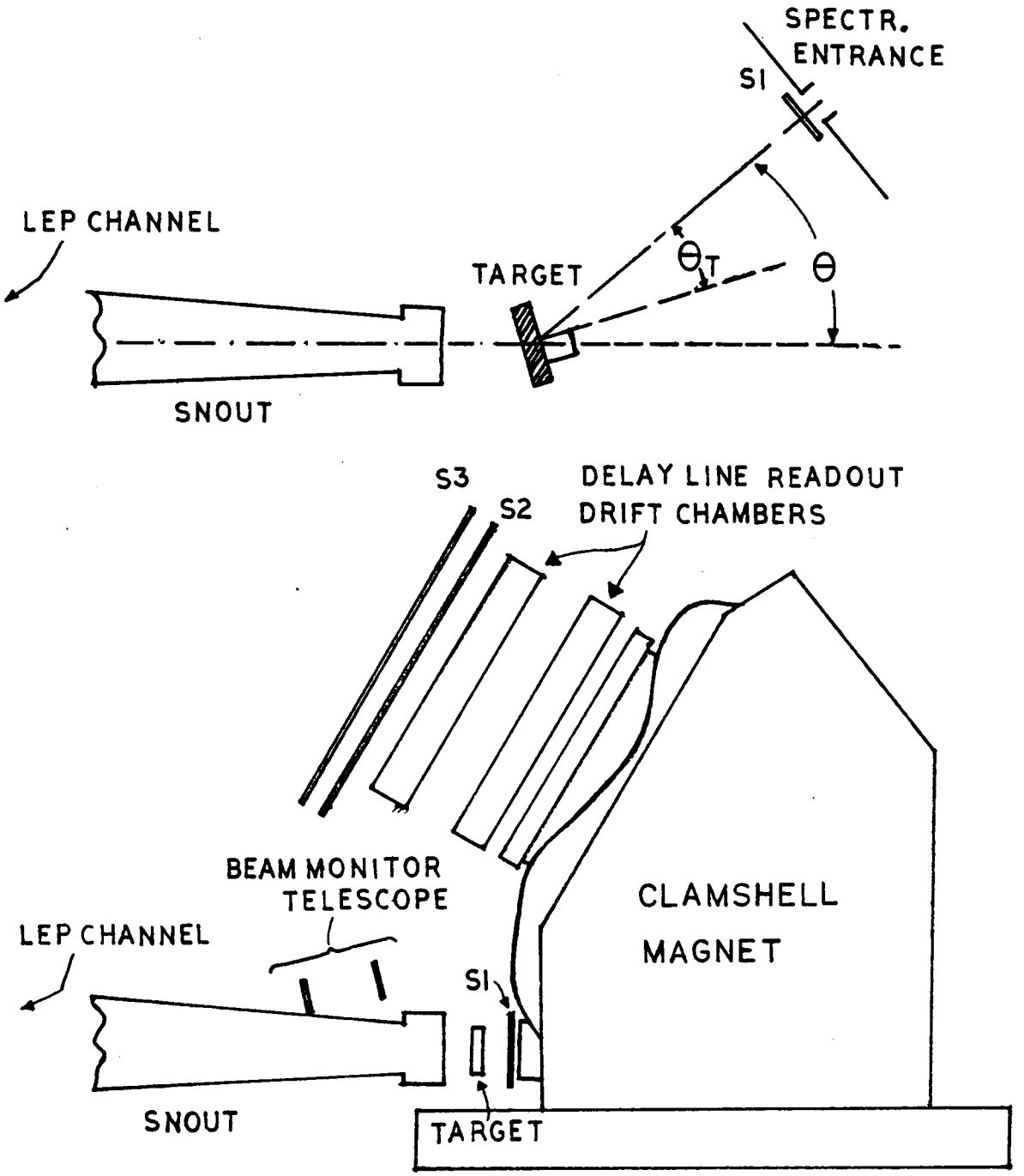

Figure II-5 Spectrometer System

Each chamber assembly is capable of measuring the intersection point of a particle in two dimensions. They consist of two separate orthogonally oriented multi-wire drift chambers of an alternate gradient design [10]. Every other wire in a wire plane is a 76 micron diameter Be-Al cathode at ground potential. The remaining wires are 20 micron diameter Gold-Tungsten anodes at positive high voltage. Each wire plane is sandwiched between 6.3 micron thick aluminized mylar foil ground planes. The inter-wire spacing is 4 mm and the wire plane to ground plane gap is 5 mm. The chambers are filled with an Argon Iso-Butane Freon gas mixture at atmospheric pressure. The entrance and exit windows , which form the gas seal for the chamber assemblies, are of 51 micron thick aluminized mylar.

As can be seen in the chamber diagram of figure II-6 the anode wires were connected to points along a delay line inside the chamber. When a signal was produced on a given anode wire by the passage of a particle it first had to travel to the junction between the wire and the delay line and then split into two signals which propagate along the delay line in opposite directions. At the two ends of the delay line the signals were each amplified and fed into seperate discriminators. The two resulting pulses, for the purposes of clarity in the rest of this thesis, are called the N-anode signal and the P-anode signal.The difference and sum of the arrival times of these signals were used to identify the wire which was closest to the particle track and the drift distance between the track and the wire respectively.

Unfortunately, this procedure, while accurately determining the absolute value of the distance of a particle track from a given anode wire, cannot

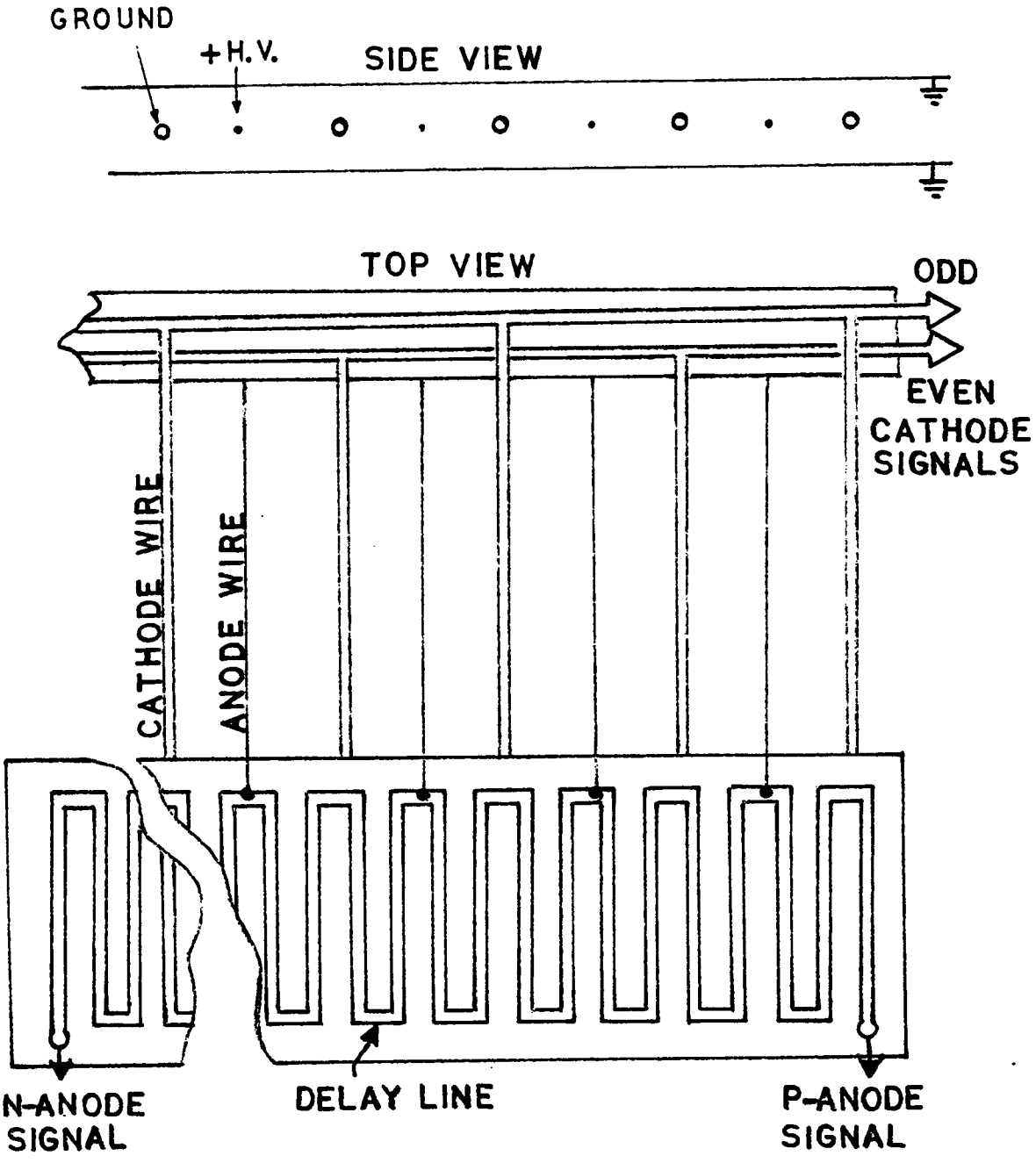

Figure II-6 Delay Line Drift Chamber Plane

unambiguously determine whether the particle had passed to the right or to the left of the wire. The usual solution to this problem is to use redundant chamber planes positioned in such a way that the wires in one chamber are offset slightly with respect to their counterparts in the other chamber. This works well for particle energies of 80 MeV or more but multiple scattering in the extra chambers begins to introduce greater and greater spread in the position measurements at lower energies. The solution is to utilize signals from the cathode wires, one of which lies between every pair of anode wires. Thus, every other cathode wire was bussed together and the two busses were connected to a voltage–sensitive differential amplifier which produced the sum and difference of the two signals (See Fig II–7). The difference signal, which shall be called the Odd–Even signal, was negative or positive depending on which side of the anode wire the particle passed.

Just behind the focal plane chambers were two scintillation counters, S2 and S3. Each of these counters covered the active area of the focal plane chambers and thus intercepted all particles which had come through the spectrometer and survived a passage through the chambers. Two phototube assemblies were attatched to each of these counters, one on each end. The timing of the signal which is called S2, for example is the hardware average of the times of the signals from its two ends. The logical "and" of signals from S2 and S3 (S2·S3) along with a signal from a 1.59 mm thick scintillation counter S1 at the entrance of the spectrometer indicated that a particle had passed from the target area through the spectrometer and through the chambers. The time delay between signals from S1 and S2·S3 provided a means of distinguishing

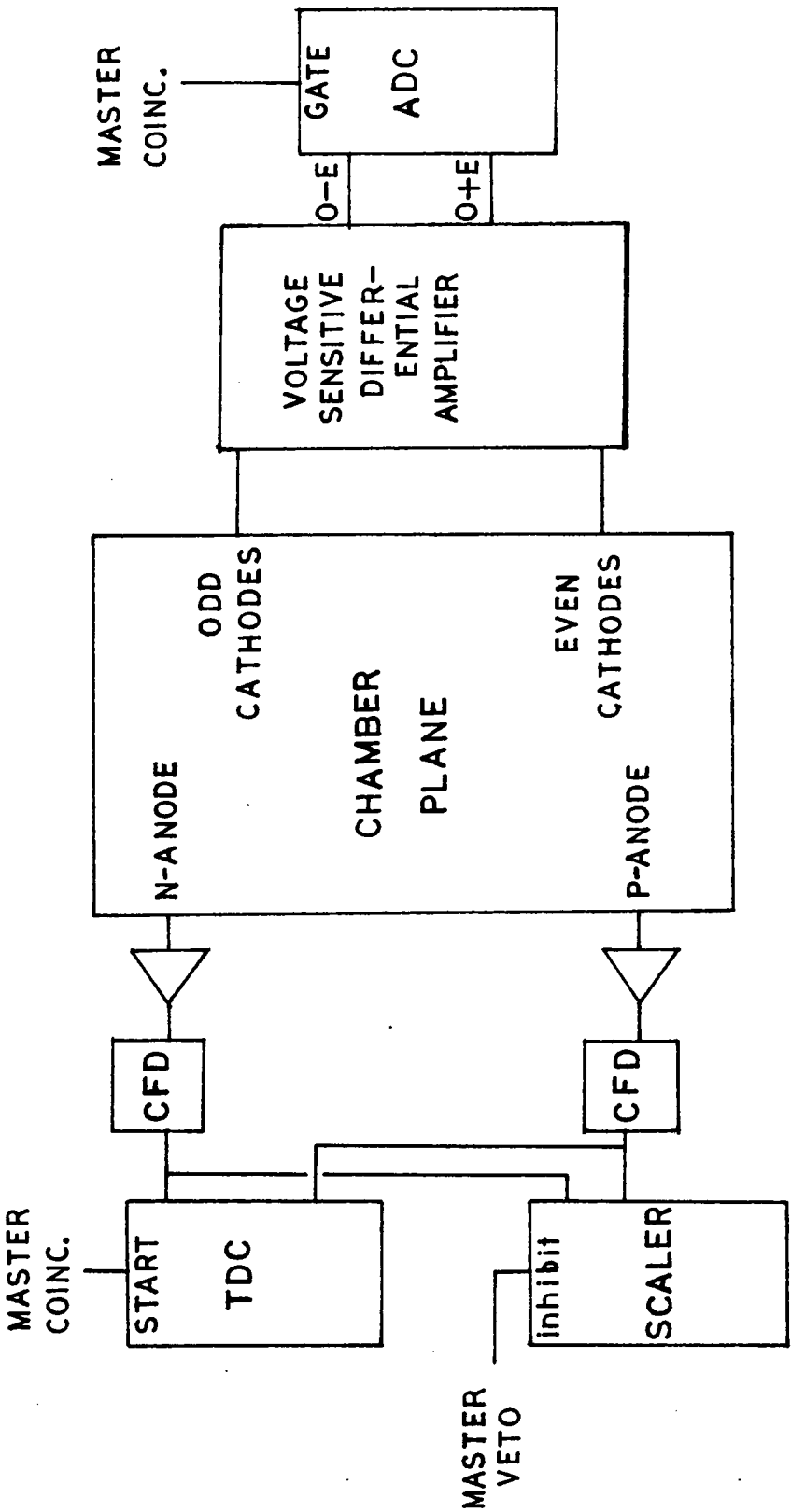

Figure II-7 Chamber readout and electronics scheme.

between pions and contaminating protons and electrons.

C. Data Acquisition

Raw signals from the S2, S3, and S1 counters along with those from the $\pi-\mu$ decay monitors and the pre-processed signals from the focal plane chambers were fed via coax cables to CAMAC modules in the LEP counting house. The chamber anode signals were fed into time to digital converters(TDCs) while the Odd-Even chamber cathode signals were fed into separate channels of an analog to digital converter(ADC). The signals from S1, S2, and S3 were split up and appropriately delayed and shaped before being input to separate ADC and TDC channels and into a logical "and" called the master coincidence (See Fig II-8). In addition to the destinations just mentioned all of the above signals were fed into scalers. The master coincidence had one additional input called the master veto which insured that the master coincidence was inhibited if certain experimental conditions were not met, such as the beam gate not being open or the magnet power supply being off. The logical signal from the master coincidence was used as a common gate for some of the ADCs , a common start for the TDCs and as a trigger to initiate the readout process (See Fig. II-7).

The interface between the CAMAC crates and the PDP 11-44 computer used in this experiment was accomplished by a standard LAMPF designed Microprogrammable Branch Driver (MBD) [11]. The MBD, upon receiving a signal from the trigger module, would read out the CAMAC modules and store

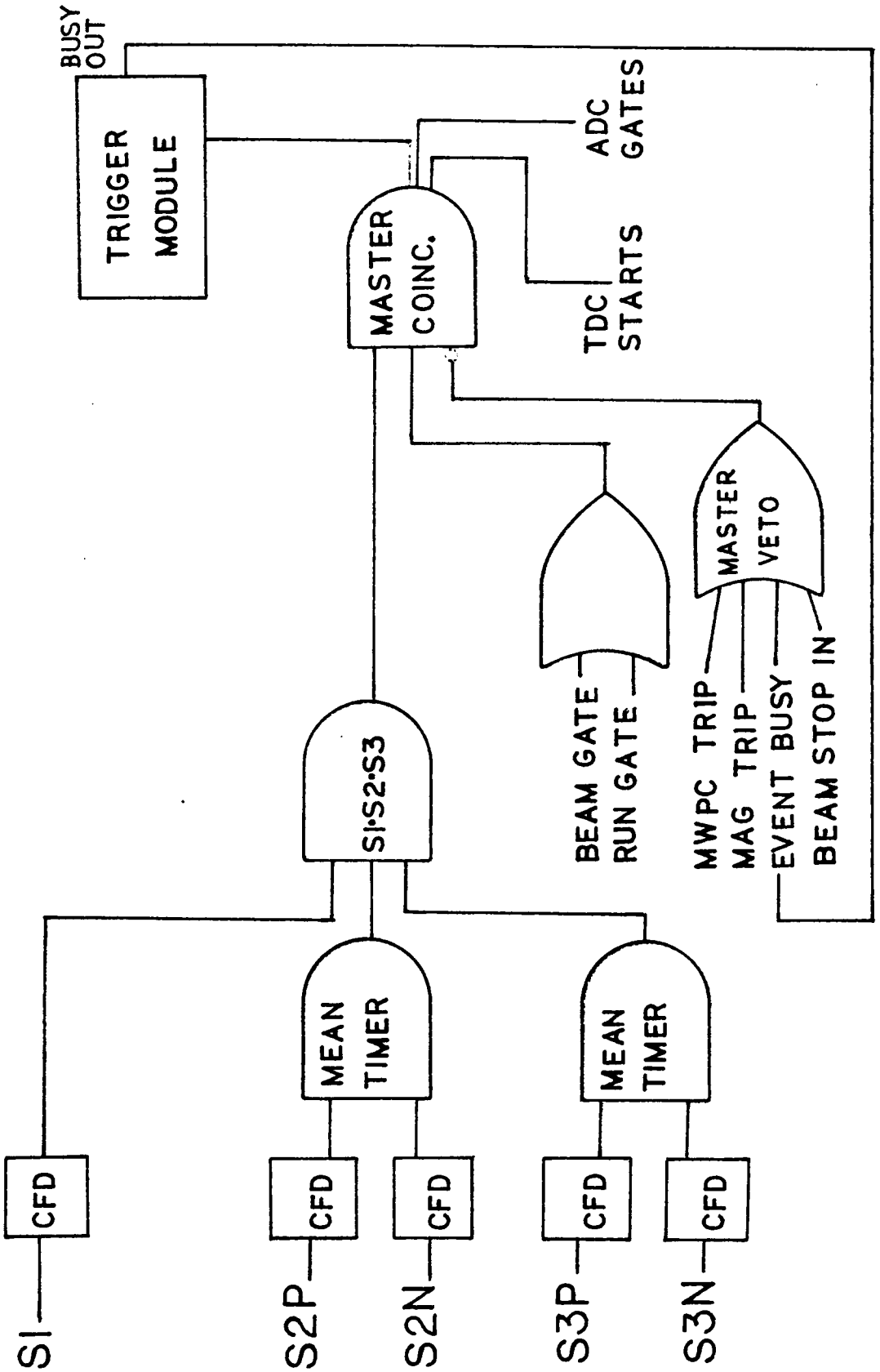

Figure II-8 Experiment trigger logic. CFD = constant fraction discriminator

the data as a block of data words in a memory buffer. The event data were then transferred to the computer when the buffer was full. This process along with many others was overseen and performed by version 2.0 of the LAMPF standard data acquisition system called the Q–system [12]. In addition to reading out the CAMAC modules in response to an event trigger the system also read out the scalers at pre–determined intervals.

Once the raw data for an event resided in the computer the Q–system began to operate on it in several ways. First, all the data words for a given event were read to magnetic tape. Secondly, a subset of the events was analyzed by a series of programs called the analyzer which converted the raw data to physical quantities of interest. The Q–system also contains programs which test the data against various criteria, and histogram both raw data and processed quantities at the request of the experimenter.

The first thing that the analyzer would do was to retrieve the event data from the memory buffer and assign variables to all the raw data quantities. Next, it calculated times and pulse heights for the signals from all the scintillators and chambers using the mean time of S2 and S3 as the reference time. This mean time was defined as the sum of the TDC values for S2 and S3 divided by two. It is a software calculation. After this the analyzer performed various tests on the new quantities in an effort to eliminate impossible or unphysical values. Next, the subroutine DCHAMBER was called. This program took raw data from each chamber and calculated a position for the particle track. For a given chamber plane it first found the crude position via the formula:

$$POS_{crude} = a_0 + a_1(N-P) + a_2(N-P)^2 + a_3(N-P)^3$$

Where N and P were the arrival times for the N-anode signals and the P-anode signals. The coefficients a_i came from a previous callibration of the delay line propagation speed [10]. Next the drift time was found by the formula:

$$T_{drift} = b_0 + b_1(N+P)$$

From the drift time the drift distance was found by reference to a lookup table which was tabulated previously. The final position was then calculated by the formula:

$$POS_{final} = POS_{crude} \pm POS_{drift}$$

The sign of POS_{drift} was determined to be positive if the ADC value of Odd-Even cathode signal was greater than a predetermined number and negative if less. Typical histograms of POS_{crude} and POS_{drift} are presented in figure II-9.

The positions derived by program DCHAMBER were then used to calculate the position and trajectory of the particle at the focal plane. It found the focal plane quantities X_{fp}, Θ_{fp}, Y_{fp}, Φ_{fp} where the first two are the position and angle in the bend plane in the dispersion direction and the second two are the position and angle in the transverse direction (See Fig. II-10). Using the knowledge of the spectrometer optics it was possible to find a particle's trajectory at the target from the measurement of its trajectory at the focal plane. The relationship between the particle trajectory at the focal plane and the target were expressed in terms of a set of polynomials. The polynomial coefficients were obtained in a callibration procedure as explained in [13]. The

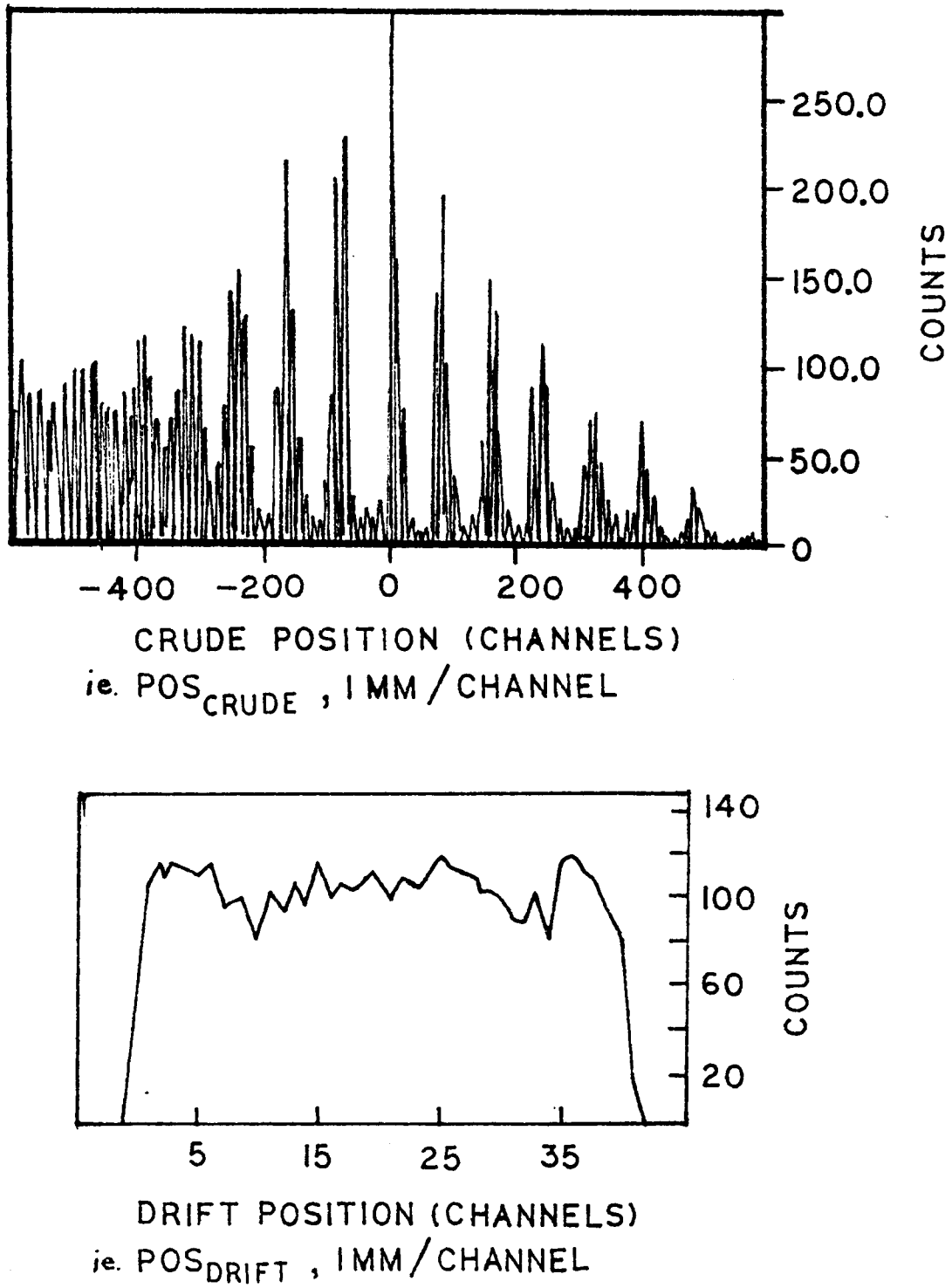

Figure II-9 Typical crude position and drift position histograms.

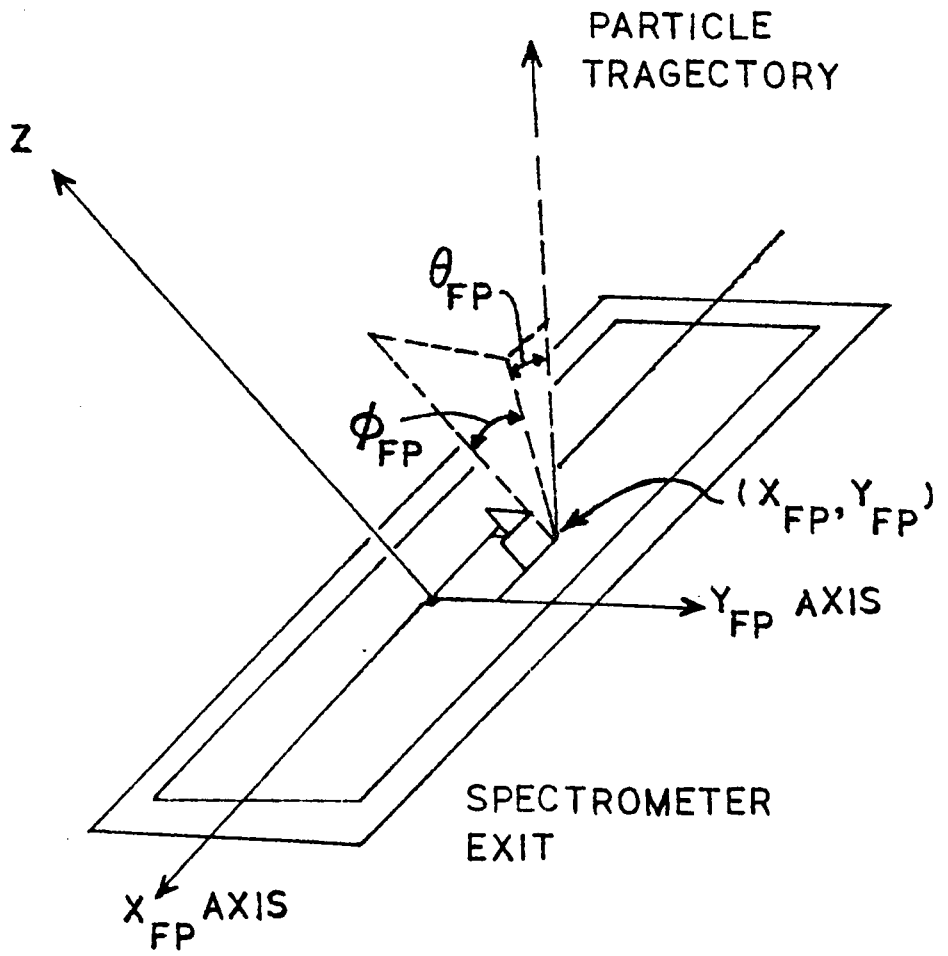

Figure II-10 Focal plane coordinate system.

focal plane quantities were thus used to find the corresponding target quantities δ_{tgt}, Θ_{tgt}, Y_{tgt}, Φ_{tgt} via the following:

$$\delta_{tgt} = P_1(X_{fp},\Theta_{fp},Y_{fp},\Phi_{fp})$$

$$\Theta_{tgt} = P_2(X_{fp},\Theta_{fp},Y_{fp},\Phi_{fp})$$

$$Y_{tgt} = P_3(X_{fp},\Theta_{fp},Y_{fp},\Phi_{fp})$$

$$\Phi_{tgt} = P_4(X_{fp},\Theta_{fp},Y_{fp},\Phi_{fp})$$

here δ_{tgt} is the difference between the particle's momentum and the central momentum (determined by the spectrometer) divided by the central momentum. The target quantities were next transformed into their rotated target frame equivalents δ_{rot}, Θ_{rot}, Y_{rot},and Φ_{rot} where, $\delta_{tgt} = \delta_{rot}$ (See Fig. II–11). This is the reference frame in which Z_{rot} is perpendicular to the plane of the target.

Program CALKIN then took the target quantities along with the spectrometer scattering angle and the incoming pion kinetic energy and performed a number of kinematic calculations. The most important quantity thus produced was the missing–mass, Q_{miss}, or residual nucleus excitation energy. It was obtained from the formula:

$$(Q_{miss}+M_D)^2 + P_D^2 = (E_{miss} + M_D)^2$$

Where,

$$E_{miss} = (T_A + M_A) + M_B - [(P_C^2 + M_C^2)^{1/2} + M_D]$$

The labeling convention used here is $Ni(\pi,\pi)Ni \longleftrightarrow B(A,C)D$, T is a particle's kinetic energy, M is it's rest mass, A, C, B and D denote the incoming particle, the outgoing particle, the target nucleus before the interaction and the target

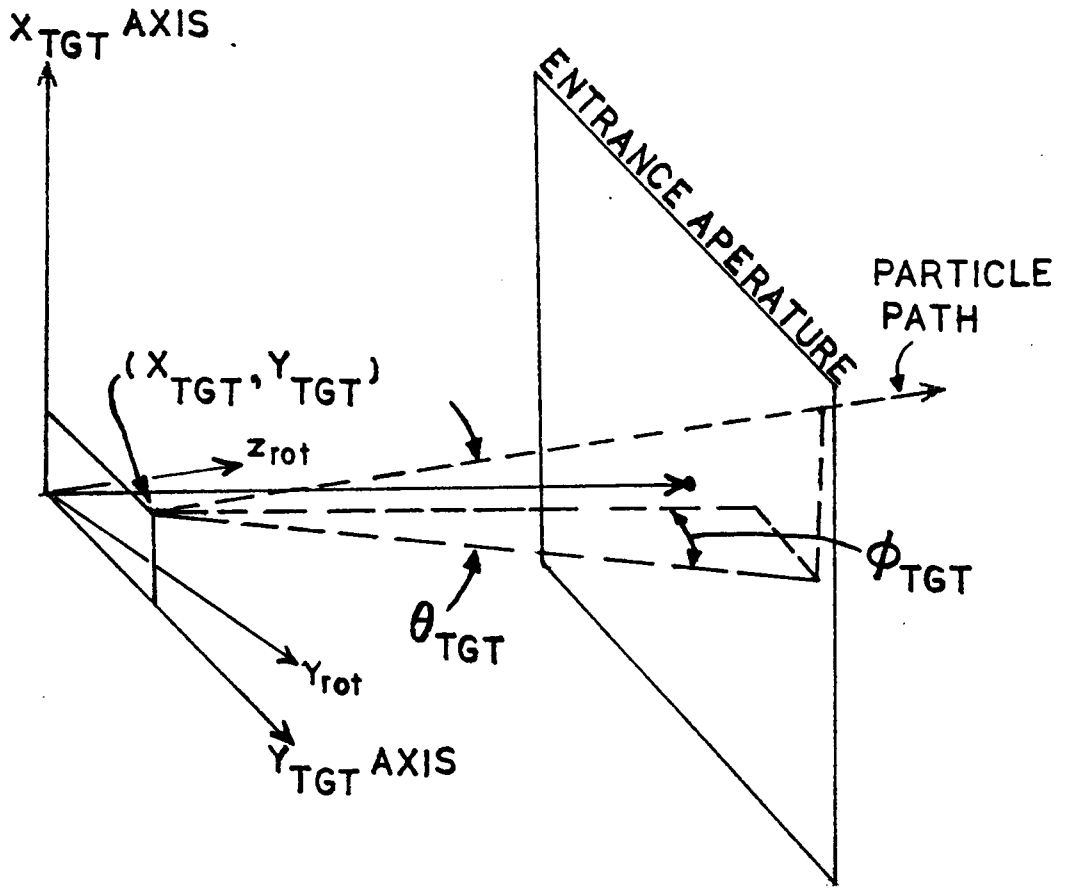

Figure II-11 Target (tgt) and rotated target (rot) coordinate systems.

nucleus after the interaction, respectively.

When an event had successfully completed its course through the analyzer the Q–system called the LAMPF Data Testing Package [14] which acts as a flexible means of classifying the data on an event–by–event basis. In addition to testing single data words (microtests) it was also possible to test logical combinations of data words (macrotests). The tests were in the form of gates which were deemed true if the data word being tested was between pre–designated limits, or boxes which were true if each of two data words fell between respective limits. All details about what tests were to be performed were specified in a user–created test descriptor file. The results of the tests were used to control whether a given histogram of a given data word should be incremented or whether a dot in a dot–plot should be plotted.

The histogramming process was accomplished by the LAMPF Histogramming and Support Package [15]. During this experiment 28 histograms were taken for each data run. Twelve of these were histograms of chamber quantities and were used during the course of the experiment to monitor the health of the equipment. The rest of the histograms were of focal plane quantities, target quantities and the missing–mass. The use of more than one histogram per data word was not uncommon since it was often of interest to observe the change produced in the histogram of a quantity when a different set of tests were applied.

Chapter III

Data Reduction

A. Tests And The Missing-Mass Histograms

The reaction yields for each run of the experiment were obtained from the missing-mass histograms which were tabulated during post-experiment replay of the data tapes. An example of one of these histograms is given in figure III-1. (Note the 600 KeV width of the peak at half-maximum.) These histograms were made up of data which had passed a series of software tests designed to sort out real events from accidental and background events. The tests fell into two main categories, chamber tests and background rejection tests.

The chamber tests were further divided into anode tests, left-right tests and drift time tests. An event was said to have passed the "GOOD ANODE" test for a given anode output if the TDC value representing the arrival time of the signal from that output fell within a set of pre-determined limits. These limits consisted simply of the range of the TDC. The "GOOD ANODE PLANE" test was passed for a given chamber plane if valid signals were registered on the outputs corresponding to both ends of the appropriate delay line. The "GOOD L-R" test was judged as passed when the ADC values of the odd-even cathode signals for all chamber planes successfully fell within pre-set limits. The lower limit was set in order to reject the "zero channel" events which

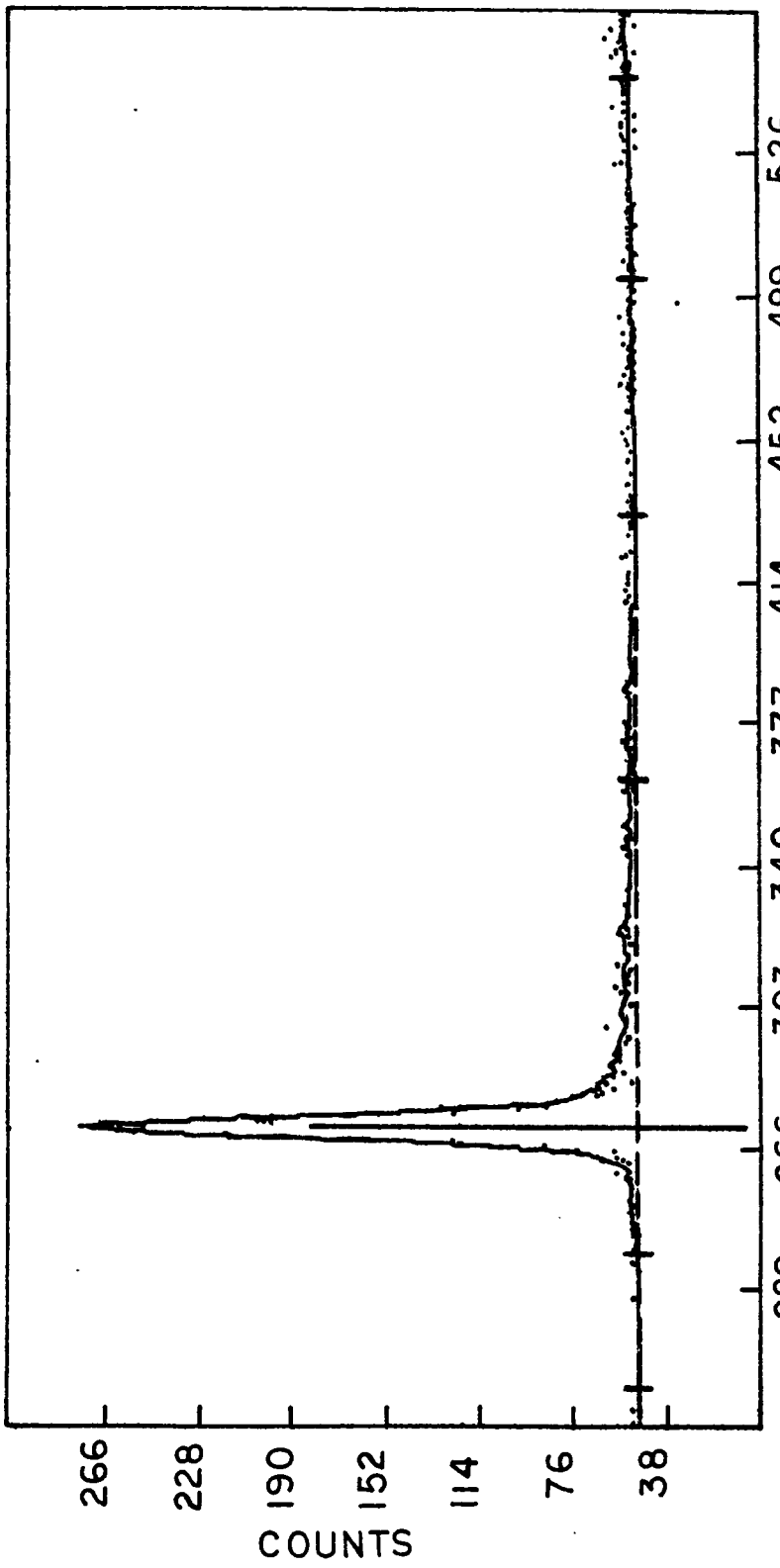

Figure III-1 Missing-mass histogram for pi- on ^{60}Ni at 65 MeV and thirty degrees. 0.1 MeV / channel. A 50 count level has been added during processing.

accumulated because of the relative inefficiency of the cathode readout scheme while the upper limit was just the maximum range of the ADC. The "GOOD CHAMBERS" test was passed when all anode outputs registered valid signals and the GOOD L–R test was successfully passed. Similarly, an event passed the "GOOD DRIFT TIME" test if the calculated drift times for all the chamber planes were less than the physically allowable maximum drift time.

The background rejection tests consisted of a series of gates on the focal plane quantities Θ_{fp}, Y_{fp} and Φ_{fp} and the target quantities Θ_{tgt}, Y_{tgt} and Φ_{tgt}. The gate limits were selected in accordance with the results of a survey of the histograms of these quantities for a representative subset of the data runs. The limits were chosen subjectively with the knowledge that the target and spectrometer geometry put definite constraints on these quantities for real events.

There were five missing–mass histograms created for each run of the experiment; MMCUT, MMASS1, MMASS2, MMASS3 and MMASS4. The MMCUT histogram contained data which was required to pass the "GRAND" test which is the combination of the "GOOD CHAMBERS", "GOOD DRIFT TIME" tests and the focal plane and target tests mentioned above. The rest of the missing–mass histograms were also gated on the "GRAND" test but with further restrictions on the quantity Φ_{tgt} (which is related to the scattering angle). The data in the MMASS1, MMASS2, and MMASS3 histograms consisted of those events with Φ_{tgt} in the angular intervals $-3.45° < \Phi_{tgt} < -1.15°$, $-1.15° < \Phi_{tgt} < 1.15°$ and $1.15° < \Phi_{tgt} < 2.45°$, respectively. The data in the MMASS4

histogram consisted of events with Φ_{tgt} in the interval $-3.45° < \Phi_{tgt} < 3.45°$.

Two major parts of the Clamshell were not operational for this first experiment; the evacuated target chamber and the focal plane muon rejector. Neither was considered essential for the experiment's success but the lack of the former necessitated the inclusion of blank (no target) runs for each spectrometer position. These blank missing-mass spectra were later scaled using the pi-mu decay monitor results and subtracted from the appropriate spectra. The Nitrogen elastic peak is for the most part not negligeable as can be seen from figure III-2. (The Nitrogen peak in this histogram is scaled up by a factor of about 2.5 for purposes of illustration.) Because of the kinematic energy shift brought about by changing scattering configurations and the behavior of its elastic cross section the Nitrogen contributed somewhat to the Nickel elastic peak at small scattering angles but much more to the first excited state at larger angles. This would make the extraction of inelastic cross sections from the data subject to rather large errors.

B. Peak Fitting

The task of extracting yields from the missing-mass histograms amounted to determining the number of counts in the elastic peak minus whatever background was present. The background consisted of events from nearby inelastic states and quasi-elastic collisions. The fitting program LOAFM was used to fit the histogram data to a peak shape taken from the data. A standard gaussian line shape was inadequate because the data clearly

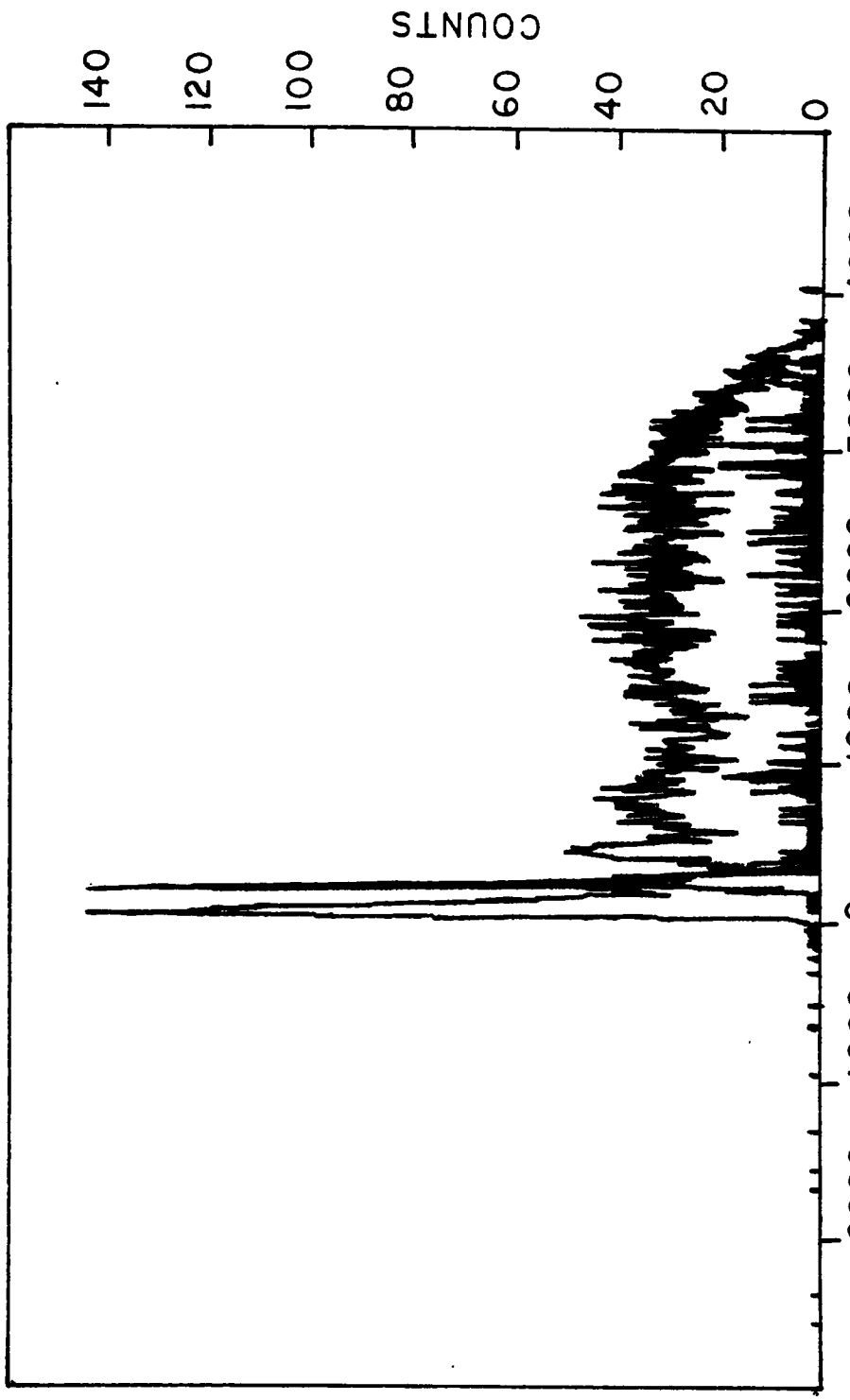

Figure III-2 Missing-mass histo. with "no target" run superimposed. 0.1 MeV / channel.

indicated the presence of a significant low energy tail as can be seen in figure III-1. The reference line shape was selected from the data in accordance with four criteria. First, there must be no visible excited states in the missing-mass spectrum. Second, the chosen peak must contain a statistically significant number of counts. Third, the low energy extent of the tail must be defineable. Fourth, the chosen reference peak shape, when used to fit a given set of data must produce a yield which is consistent with the yield produced when using other candidate reference peak shapes. The candidate reference shapes had to be chosen by the first three criteria listed above. The collection of reference shapes investigated produced yields which were consistent among themselves to within two percent.

LOAFM was capable of fitting up to ten peaks in a single histogram simultaneaously while subtracting a user defined background. The definition of the the background was done by the experimenter following the two rules : 1. the background is zero at the position of the elastic peak and at higher energies 2. at energies below that of the elastic peak the background must smoothly rise to the level of the quasi-elastic part of the spectrum.

C. The Differential Cross Sections

The number of elastically scattered pions detected at the focal plane of the spectrometer is given by :

$$N_{EL}(E,\Theta) = \frac{N_{pi-mu} \cdot SF \cdot f \cdot \varepsilon \cdot \Delta\Omega N_{tgt} \cdot d\sigma_{EL}/d\Omega \cdot}{CORR}$$

Where Θ is the scattering angle, N_{pi-mu} is the number of counts (coincident−random) seen by the beam monitor during the live time of a run. f is a constant of proportionality which relates the number N_{pi-mu} to the number of pions on target. N_{tgt} is the number of target nuclei intercepted by the beam per unit area.

ie. $N_{tgt} = \rho \cdot t \cdot N_A / A \cdot \cos(\Theta_t)$

Where ρ is the target mass density, t is its thickness, N_A is Avagadro's number, A is the atomic mass and Θ_t is the angle between the beam direction and a line normal to the target (the target angle, usually $\Theta/2$). $d\sigma_{EL}/d\Omega$ is the lab elastic differential cross section. $\Delta\Omega$ is the spectrumeter solid angle. ε is a measure of the overall efficiency of the detection system. SF is the fraction of pions which do not decay into muons while inside the spectrometer.

$$SF = \exp\left(m_{pi} \cdot \text{Path Length} \;/\; p_{pi} \cdot \text{Ave Decay Length}\right)$$

CORR is the run−specific efficiency correction factor given by

$$CORR = (\text{Computer Live Time} \cdot \text{Chmbr Eff} \cdot \text{Dreff} \cdot \text{LP/EV})^{-1}$$

The quantities in parentheses are defined below. If an event is defined as a master coincidence which is accompanied by a run gate and a beam gate, then the computer live time is just

$$CLT = \frac{\text{number of EVENTS} \cdot \text{computer NOT busy}}{\text{number of EVENTS}}$$

This ratio yields the fraction of events for which the computer was not busy. The term LP/EV is an indicator of the efficiency with which the analyzer task

is being called when valid events are present. It is calculated as follows :

$$\text{LP/EV} = \frac{\text{number of calls to the analyzer task}}{\text{number of EVENTS} \cdot \text{computer NOT busy}}$$

Chmbr Eff or chamber efficiency is the product of the two efficiencies Reff and Feff which are calculated as follows :

$$\text{Reff} = \frac{(\text{number passing X1 ANODE PLANE test})^2}{\text{X1N ANODE test passed} \cdot \text{X1P ANODE test passed}} \times (\text{Same For The Other Planes})$$

and

$$\text{Feff} = \frac{\text{number of events passing GOOD CHAMBERS test}}{\text{number of calls to the analyzer task}}$$

The term Dreff is the drift efficiency or the fraction of events in which all the chambers fired but did not pass one or more of the drift time tests :

$$\text{Dreff} = \frac{\text{number passing GOOD CHAMBER and DRIFT TIME tests}}{\text{number passing GOOD CHAMBER test}}$$

Some values of the above quantities are plotted versus scattering angle in figure III–3.

The elastic differential cross section in the center of mass frame is thus:

$$\frac{d\sigma_{(cm)}}{d\Omega} = \frac{G \cdot N_{EL} \cdot CORR}{N_{tgt} \cdot N_{pi-mu} \cdot SF} \quad \frac{1}{(f \cdot \varepsilon \cdot \Delta\Omega)}$$

Where G is the jacobian transformation from the lab to the center of momentum frame. The term $(f \cdot \varepsilon \cdot \Delta\Omega)^{-1}$ is a constant for the spectrometer and is found by normalizing to known Hydrogen cross sections. This will be dealt with

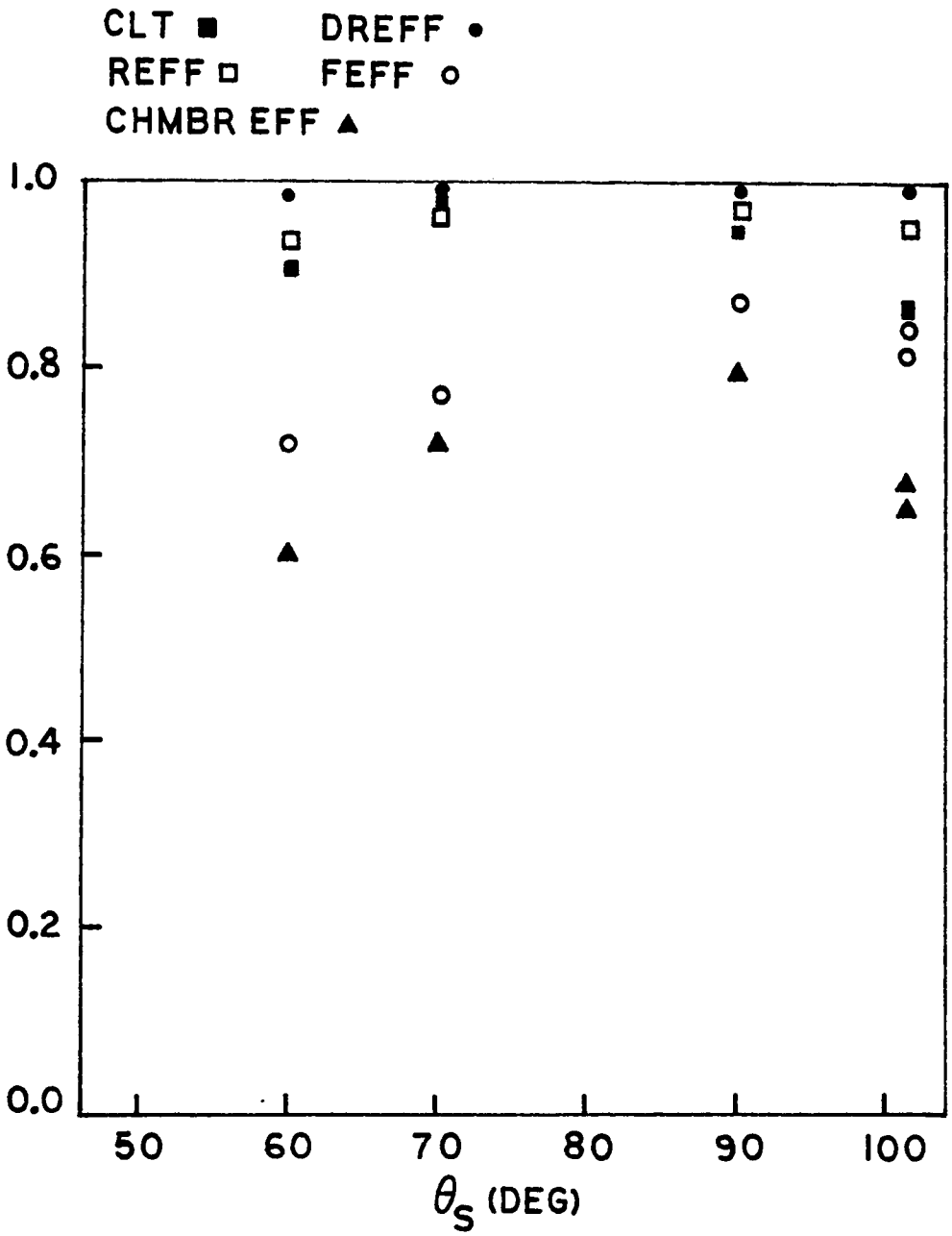

Figure III-3 Chamber efficiencies vs. scattering angle.

in section D of this chapter.

The Nickel differential cross sections have rather deep minima which occur between the scattering angles of 80° to 100°. In order to better explore this important region three cross sections were calculated for every run having a scattering angle in this range. Each of the three cross sections covered an angular region or bin of 2.3°. The three regions were adjacent but non-overlapping with the central region centered at $\Phi_{lab} = 0°$. The reaction yields for the cross sections were extracted from the three missing-mass histograms, MMASS1,MMASS2, and MMASS3. In order to correct for the fact that only part of the angular acceptance of the spectrometer was used in obtaining the data in the MMASSn (n=1,2,3) histograms, the normalization constant RATIO = $(f \cdot \varepsilon \cdot \Delta\Omega)^{-1}$ had to be modified by the multiplicative factor α_{MMASSn} for each of the three cross section calculations. As a first step in finding this factor the Φ_{lab} histogram obtained from a run using a ^{12}C target was suitably scaled and subtracted from the Φ_{lab} histogram obtained from a corresponding run using a CH_2 target. The result, which is shown in figure III-4 is a representation of the angular acceptance of the spectrometer convolved with the π^+-p cross section. Since the cross section changes by less than 4% across the selected range of Φ_{lab} its deconvolution with the angular acceptance was not attempted. The normalization correction factor α_{mmassn} was obtained by dividing the total number of counts in the Φ_{lab} histogram by the number of counts in the given angular range used in tabulating the MMASSn histogram. Thus, the cross

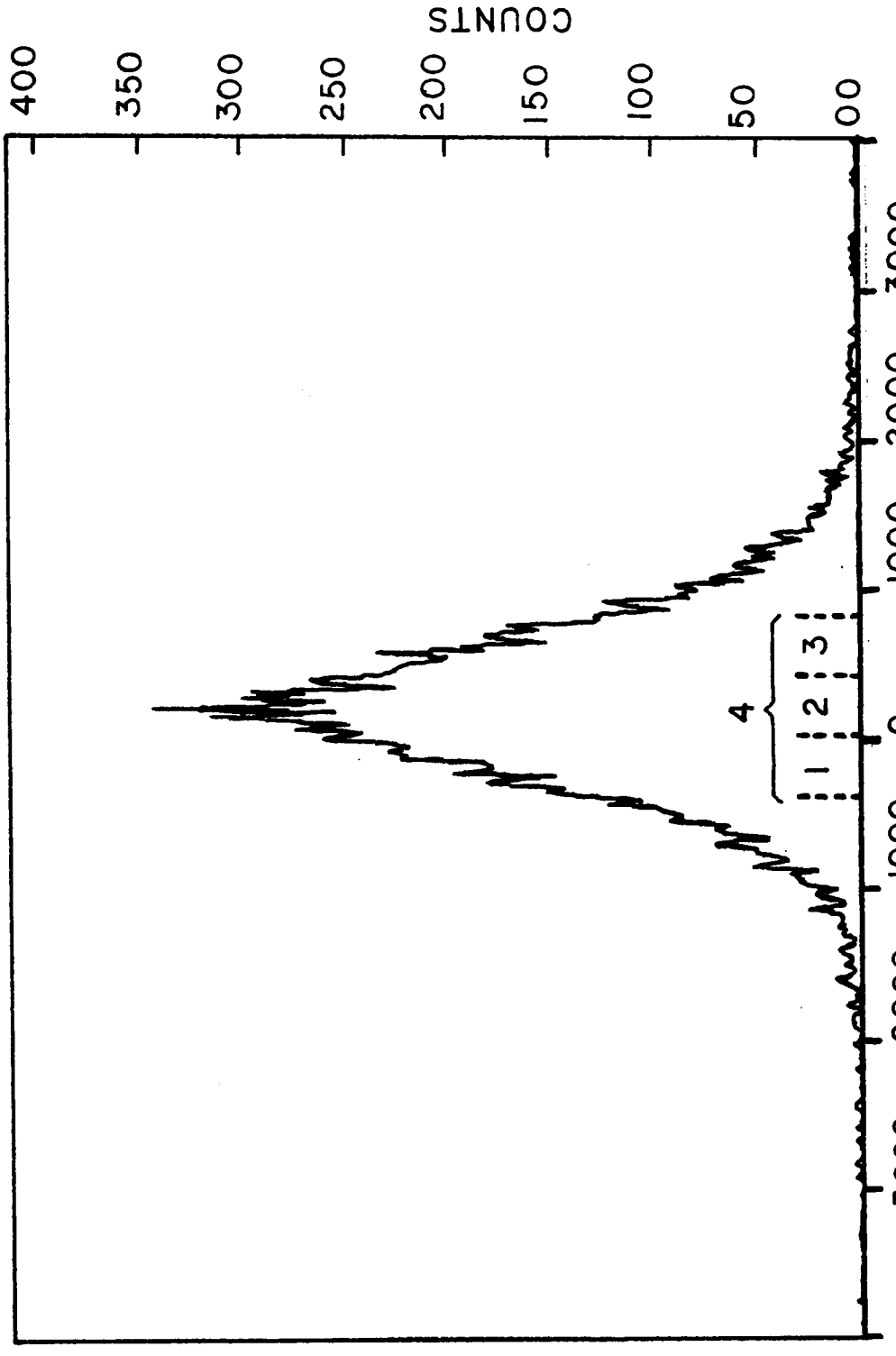

Figure III-4 histogram with angular bins 1,2,3 indicated. 10 chans. / mrad.

section for a given angular bin was calculated using the following formula :

$$\frac{d\sigma_{(cm)}}{d\Omega} = \frac{G \cdot N_{EL} \cdot CORR}{N_{tgt} \cdot N_{pi-mu} \cdot SF} \cdot \frac{1}{(f \cdot \varepsilon \cdot \Delta\Omega)} \cdot \alpha_{MMASSn}$$

D. Normalization To Hydrogen

Normalization of the differential cross sections was achieved by taking scattering data from CH_2 and ^{12}C targets during the course of the experiment. The scattering angles for which this was done were 50, 55, 60, 70, 90 and 100 degrees. Both π^+ and π^- data were obtained at 65 MeV and one π^- measurement at 90 degrees was taken at 50 MeV. The missing–mass histograms were then obtained in the usual manner during data replay. A pure Hydrogen missing–mass spectrum was produced by subtracting the suitably scaled ^{12}C histogram bin by bin from the corresponding CH_2 histogram. The experimental yield was extracted by summing the Hydrogen histogram between limits which were selected so as to contain the elastic peak and its low energy tail as can be seen in figure III–5.

The quantity $(f \cdot \varepsilon \cdot \Delta\Omega)^{-1}$ which is supposed to be constant for all scattering angles at a given energy on the spectrometer was obtained using the following expression :

$$(f \cdot \varepsilon \cdot \Delta\Omega)^{-1} = RATIO = \frac{d\sigma_H(\theta)}{d\Omega} \cdot \frac{N_{pi-mu} \cdot N_{tgt} \cdot SF}{N_{EL(H)} \cdot CORR}$$

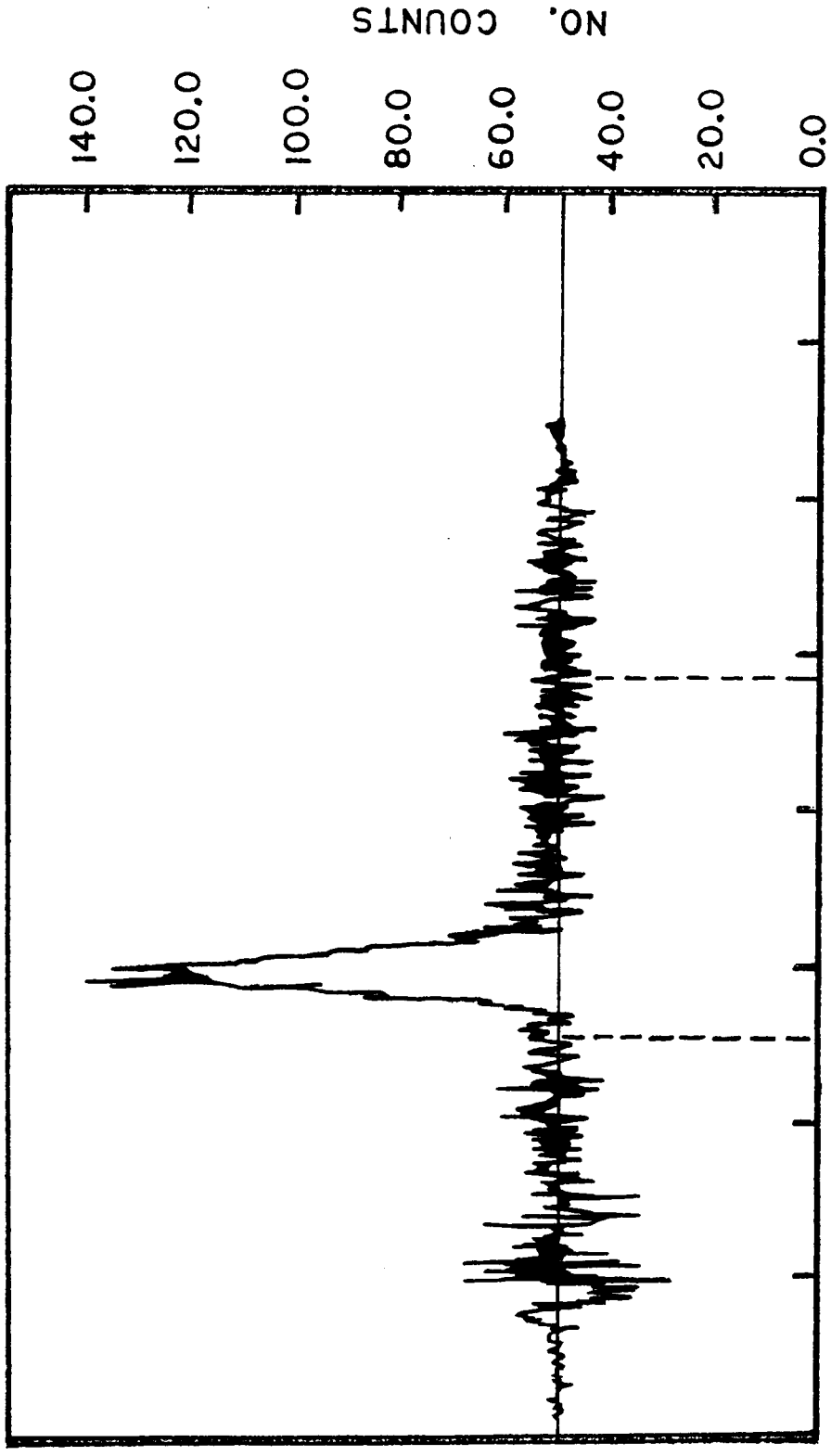

Figure III-5 Typical Hydrogen missing-mass histogram. 0.1 MeV per channel.

Here, $d\sigma_H(\Theta)/d\Omega$ is the π-p differential cross section derived from phase shifts [16] and transformed to the lab frame. $N_{tgt} = 2 \cdot \rho t \cdot N_A$ / $14 \cdot \cos(\Theta_t)$, since there are two H-atoms per CH_2 molecule. In order to get an idea of the normalization error the quantity $RATIO^{-1}$ was calculated for all the CH_2 runs and plotted in figure III-6. This plot includes both π^+ and π^- data taken at 65 MeV. The value chosen for $RATIO^{-1}$ was 0.11 which was the average of the data points and the standard deviation of the set of data points from the average was 6.0 %. This was taken as the absolute normalization error. The error bars associated with each point were calculated from the the number of counts constituting the reaction yield for each. Thus, the statement that the quantity $(f \cdot \varepsilon \cdot \Delta\Omega)^{-1}$ is independent of scattering angle is consistent with the data since the error bars of all the points were within one sigma of the average. The normalization for the 50MeV data was obtained from only one data point at 60°. The error in this measurement, as determined from the counting statistics of the yield was 6.8%. The value of the 50MeV normalization constant $RATIO^{-1}$ was 0.19.

E. Estimation Of Errors

The errors quoted for the data in this thesis stemmed primarily from the various uncertainties in the determination of the reaction yields. The statistical and fitting errors were estimated by the fitting program LOAFM. The fitting errors were based on the χ^2 of the fit and the statistical errors were based on

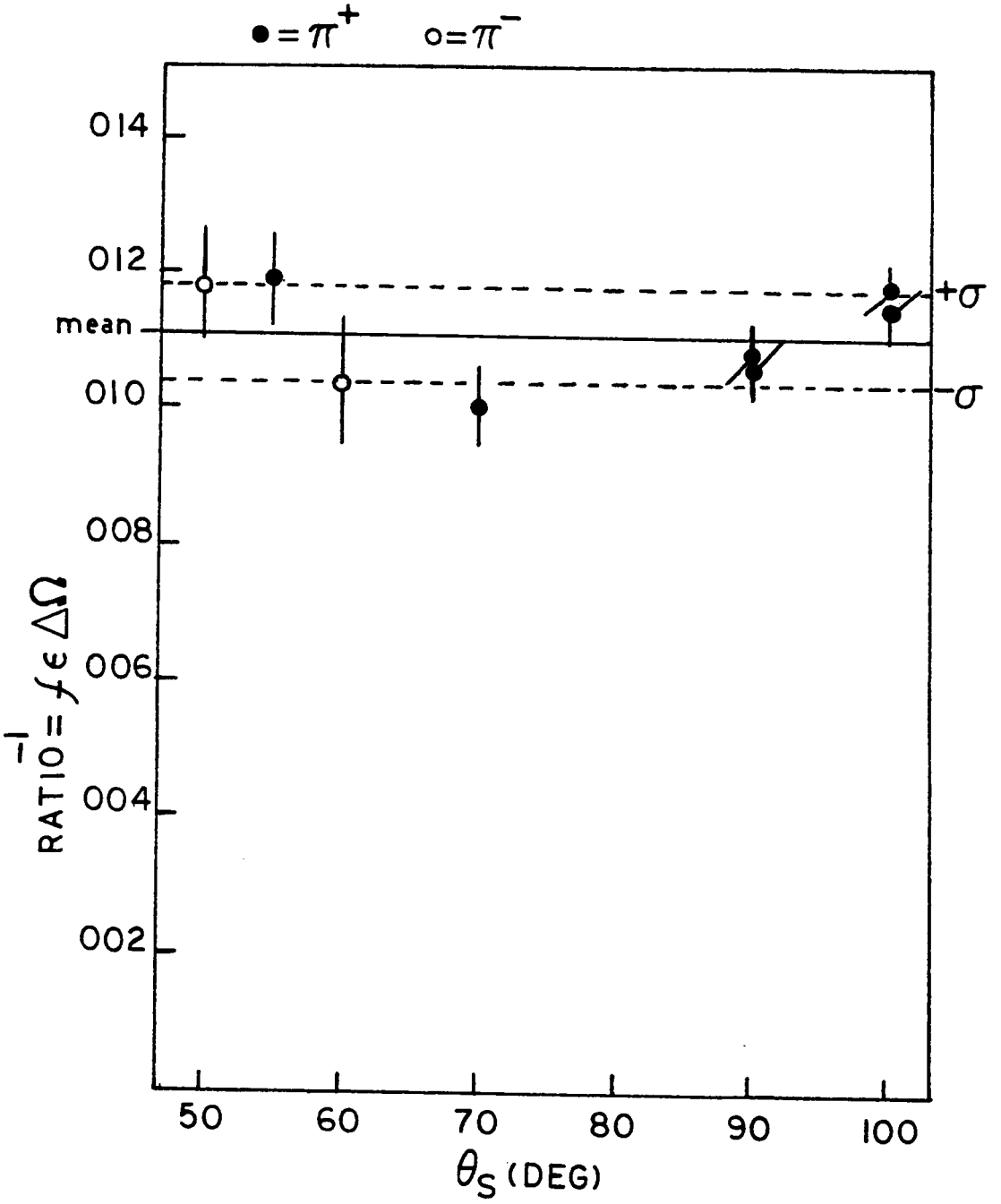

Figure III-6 The cross section normalization constant $RATIO^{-1}$ obtained from pion-Hydrogen scattering at various scattering angles.

elastic peak counting statistics. Since the missing-mass histograms from which the yields were extracted were the result of a subtraction of the Nitrogen scattering data it was necessary to include the counting statistics of the subtracted part in the error calculation as well. These contributions were added together in quadrature. Combined with all this was the 2% uncertainty which arose from the process of defining the background during the fitting procedure. This figure was reached after trying various resonable background definitions for the same spectrum and then determining the spread in the values of the resulting yields. Related to this was the 2% spread in yields obtained when using different reference peaks to fit the same data. The criteria for the selection of these peaks was outlined in section B.

Another source of error was the determination of the target angle Θ_t. It was estimated that the experimenter could only position the target to within 0.5°. The resulting percent error was calculated using :

$$\frac{\Delta\sigma}{\sigma} = \tan(\Theta_t)\cdot\Delta\Theta_t$$

The scattering angles used in the experiment ranged from 15° to 45° so the percent error due to target angle uncertainty never exceeded 1.5%. For the most part this was insignificant with respect to the other errors arising from other sources.

There were other sources of error which were not included because they were too small. One of these was the statistical error associated with determining N_{pi-mu}, the number of decay muons registered in the beam monitor during the run. For a typical run this effect contributed about 0.1% to the error.

Another possible source of systematic error was the effect which the beam muon contamination had on determining the yield. About 10% of the beam at the target consisted of muons of the same momentum as the pions in the beam [6]. At small angles these muons could be strongly coulomb scattered by the target and pass into the spectrometer to be counted as pions at the focal plane. There were two reasons why this effect was small, however. First, the beam muons, unlike the beam pions, were spread out in a 10 cm by 10 cm halo at the target and second, the smallest scattering angle used in the experiment was 30 degrees. Since the target was only 7 cm by 4 cm in size only about 28% of the muons were capable of being scattered. Thus, only 2.8% of the beam on target consisted of muons. The coulomb cross section at 30° for a Z=28 nucleus is about 60 mb/sr while the π^+ cross section taken from the present data is about 200 mb/sr. The ratio of the number of muons to the number of pions at the focal plane is thus $0.028 \times 60/200 = 0.008$ or less than 1%.

F. Finite Solid Angle and Target Spot Correction

Where the cross section changes rapidly with scattering angle the finite width of the spectrometer entrance and the finite size of the target spot introduce a systematic error in the cross section measurement. The data must be corrected to account for the difference between scattering from a finite target spot into a finite aperature and scattering from a point target spot into a point aperature. The corrections for a rectangular aperature is given below (See Appendix A for explanation).

$$\sigma_c = \sigma_m - \sigma'_m[\ \frac{\cos(\Theta)}{6}(\Delta_X^2+\Delta_Y^2+\Delta_U^2) + F_V\Delta_V^2\ ]$$

$$- \sigma''_m[\ \frac{(1-\cos^2(\Theta))}{6}\Delta_Y^2 + G_V\Delta_V^2\ ]$$

$$F_V = \frac{-\cos(\Theta)(1-7\sin^2(\Theta-\Theta_t))/6 + \sin(\Theta_t)\sin(\Theta-\Theta_t)}{\cos^2(\Theta_t)}$$

$$G_V = \frac{\cos^2(\Theta)\sin^2(\Theta-\Theta_t) + 2\cos(\Theta)\sin(\Theta_t)\sin(\Theta-\Theta_t) + \sin^2(\Theta_t)}{6\cos^2(\Theta_t)}$$

Where σ_c is the corrected differential cross section, σ_m, σ'_m and σ''_m are the measured differential cross section and its first and second deravitives at the scattering angle Θ. Θ_t is the target angle. Δ_X and Δ_Y are the vertical and horizontal aperature dimensions in units of the target to aperature distance. Δ_U and Δ_V are the vertical and horizontal rms values of the beam spot dimensions in units of the target to aperature distance.

For runs having the special scattering angles between 80° and 100°, where the angular acceptance was divided into three parts with a cross section calculation for each part, a different procedure was needed. Since the data which made up the cross sections was specifically cut on angle for these runs the systematic error arises because of the finite angle bins(2.3°) used and not from the finite beam spot or spectrometer entrance aperature. The following formula was used to make the correction :

$$\sigma_c = \sigma_m - \sigma'_m[\ \frac{X_2^2-X_2^2-X_0}{2(X_2-X_1)}\ ] - \sigma''_m[\ \frac{X_2^3-X_1^3}{3(X_2-X_1)} - X_0\frac{(X_2^2-X_1^2)}{X_2-X_1} + X_0^2\ ]$$

$X_1 = \cos(\varphi_0 - \Delta\varphi/2)$ $\quad X_2 = \cos(\varphi_0 + \Delta\varphi/2)$

φ_0 = scattering angle at center of bin, $\Delta\varphi$ = bin width

For both procedures it was necessary to first find an algebraic representation of the un-corrected data. This was done by fitting the data to a phase-shift expansion. First and second derivatives of the expansion were then calculated and inserted into one or the other of the above two formulae. Typically, the corrections in the cross sections were 10% or less.

In addition to the corrections made above there were also corrections made for the finite beam angular divergence and multiple scattering in the target. Each of these effects increases the uncertainty in the knowledge of the scattering angle which is the same thing as increasing the width of the angular acceptance bin. In the case of multiple scattering in the target the effective width of the bin is given by the standard formula for the rms multiple scattering angle. For the beam divergence the effective angular bin was given by the FWHM horizontal beam divergence angle as given in [6].

Chapter IV

Data Analysis and Theoretical Interpretation

A. The Data

The differential cross sections obtained in the experiment are tabulated in tables B–1 through B–6 and displayed in graphical form in figures IV–1 thru IV–4. The errors quoted for the cross sections do not include the 6% absolute normalization error for the 65 MeV data or the 6.8% absolute normalization error for the 50 MeV data. There was, in addition some 65 MeV data taken at 117° which was not included in the tables because of questions about its trust–worthiness. At scattering angles above 110° a depression in the side of the clamshell magnet which was designed for purposes of clearance would partially enclose the beam pipe. Unfortunately the depression was found to also contain a very strong magnetic field which could have adversely affected the path of pions on target.

The most obvious characteristic of the 65 MeV π^+ elastic cross sections as seen in figure IV–1 is the striking similarity between the three curves for ^{58}Ni, ^{60}Ni and ^{64}Ni. Only at smaller angles do the cross sections begin to differ noticeably beyond their uncertainties. The second characteristic of note concerning the π^+ cross sections is their very deep and narrow first minimum. The finite solid angle correction process was hindered for some scattering angles near the cross section minimum due to this depth and narrowness. In particular

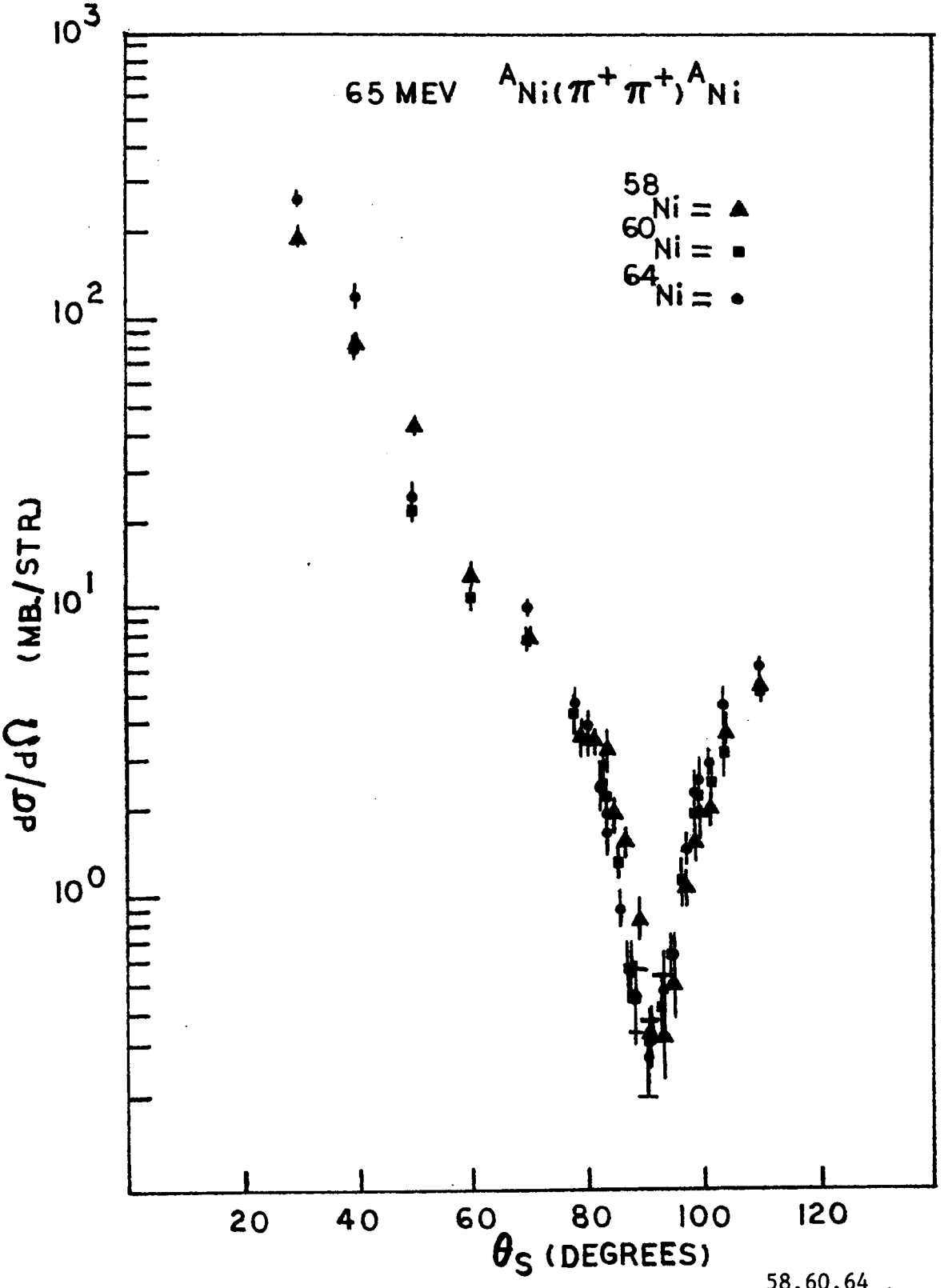

Figure IV-1 65 MeV pi+ elastic cross sections. $^{58,60,64}Ni$.

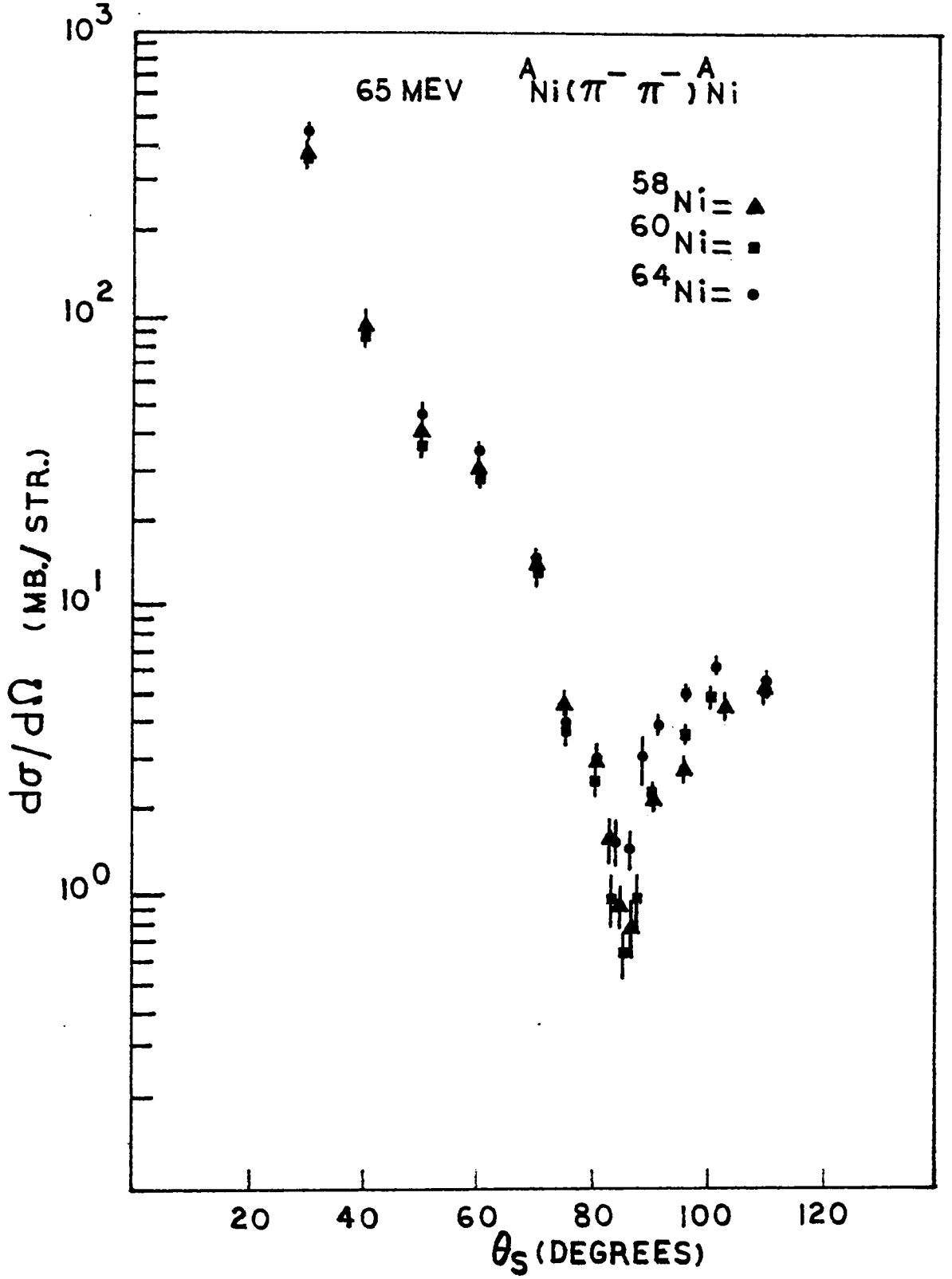

Figure IV-2 65 MeV pi- elastic cross sections.

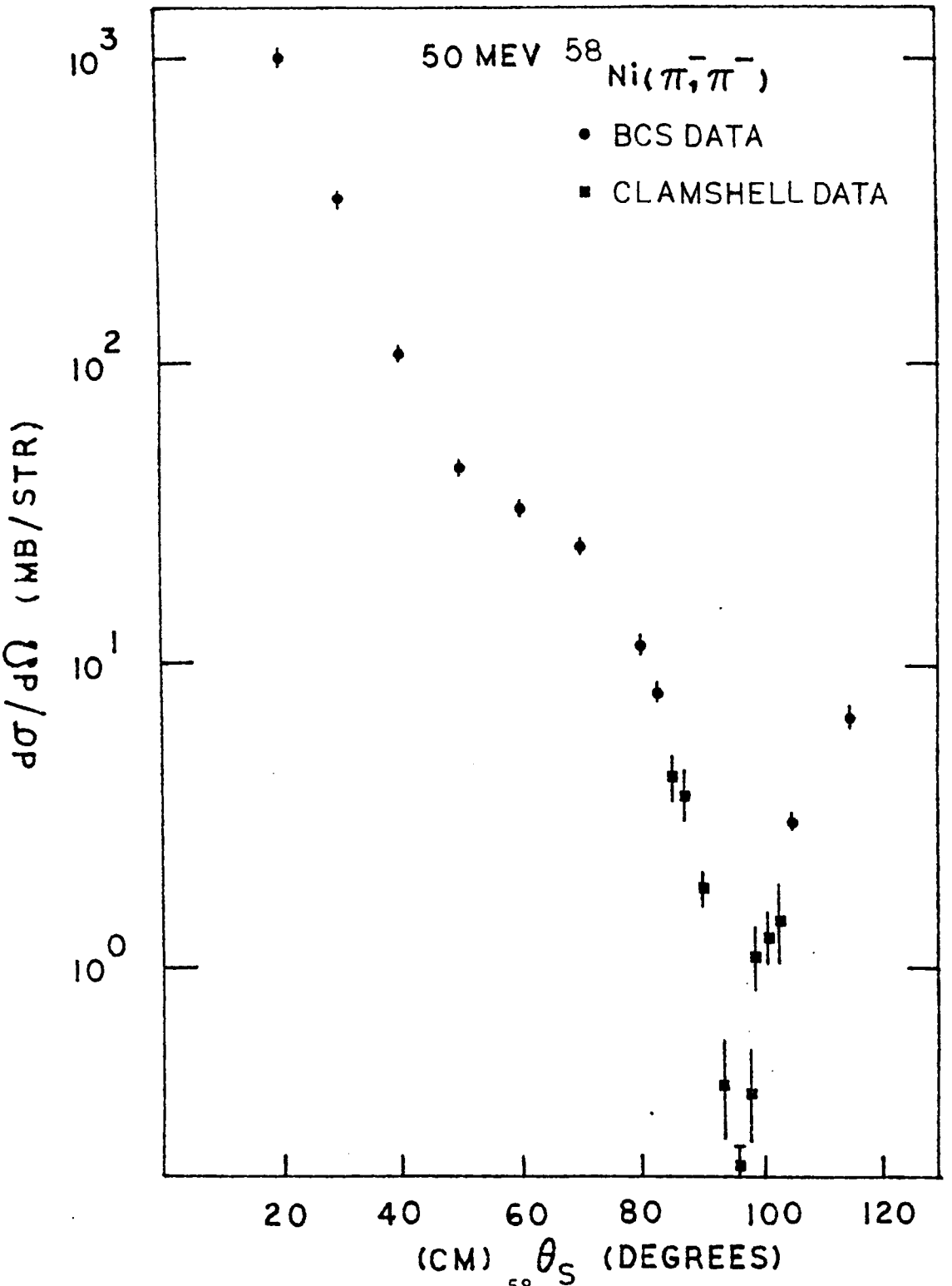

Figure IV-3 50 MeV pi- ^{58}Ni elastic cross section.

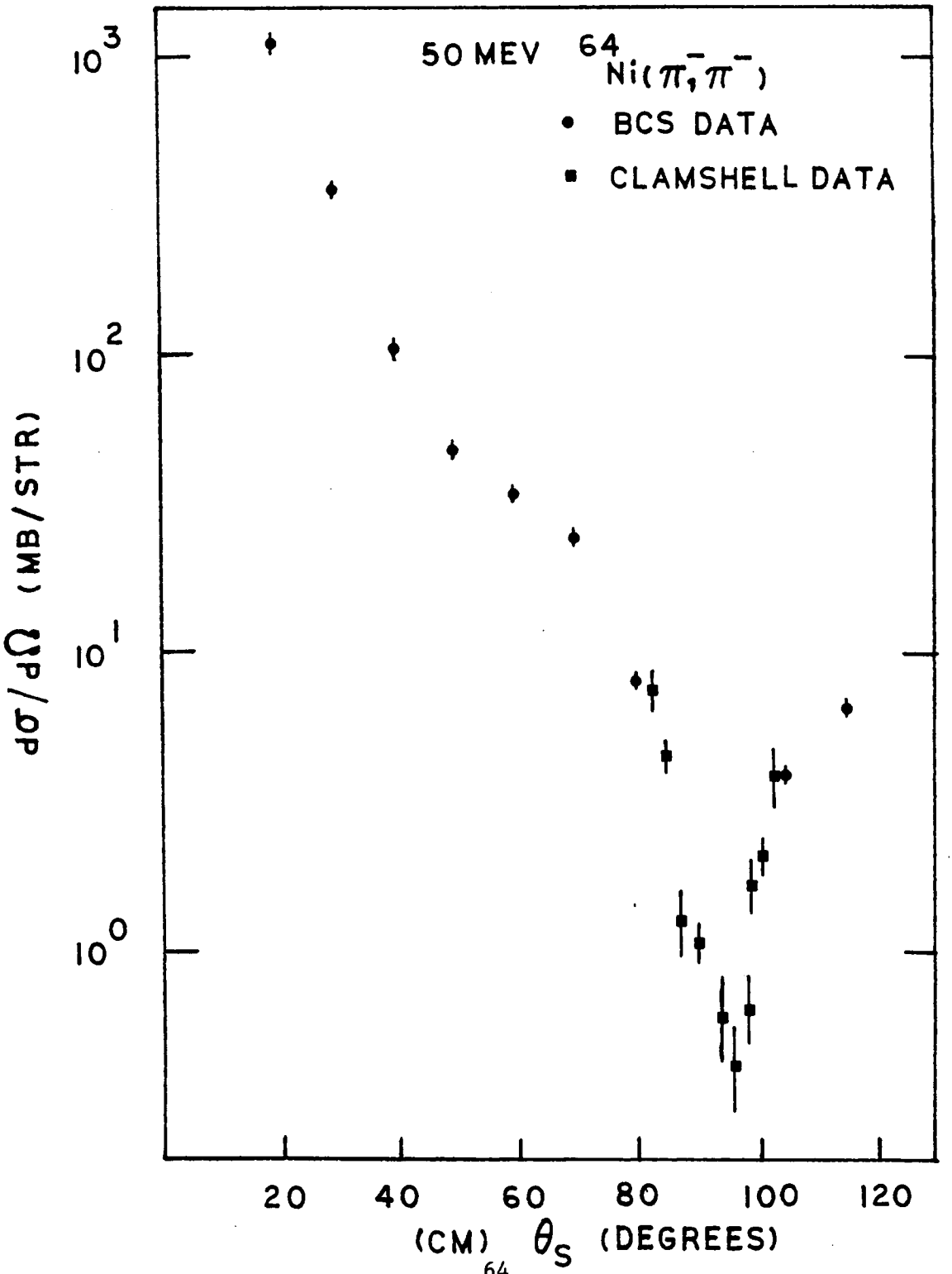

Figure IV-4 50 MeV pi- ^{64}Ni elastic cross section.

the ^{60}Ni and ^{64}Ni data contain some points which are shown with horizontal error bars. The finite solid angle correction for these points exceeded 50% of the measured cross section so the corrected values were not used. The horizontal error bars are indicators of the angular bin width used (2.3°).

The 65 MeV π^- cross sections are shown in figure IV–2. It can be seen that the minima are less deep than in the corresponding π^+ data. This situation of deep minima for π^+ data and shallower minima for the π^- is the reverse of what occurs at 50 MeV. Also, in the π^- data one sees that past a scattering angle of 90° the curves for the different isotopes begin to differ significantly from each other. This isotopic spin difference dependence is most pronounced between the angles of 85° and 105°. At forward angles the curves are almost identical.

The 50MeV data taken during the experiment is shown in figures IV–3 and IV–4. These data were taken for the primary purpose of supplementing the data which were obtained using the Bicentennial spectrometer(BCS) during a previous experiment [4]. The BCS data lacked coverage in the angles immediately surrounding the first minimum of the cross section so the data taken in the present experiment were confined to this 15° region. Also, because of time constraints and very low event rates at the chosen angles only ^{58}Ni and ^{64}Ni targets were used. It is easily seen in the figures that the new data points smoothly join to the BCS data within the error of the measurements. This consistency between the two data sets indicates that the Clamshell spectrometer is working and that the associated data reduction techniques were correctly

executed. The BCS data, if taken by itself leads one to the false conclusion that the minimum for ^{64}Ni occurs at a smaller angle and is shallower than the minimum defined by the new data. Similarly, the BCS data implies a shallower minimum for the ^{58}Ni cross section than is defined by the new data. The position of the minimum for ^{58}Ni , however, is unaffected by the new data. Thus, the isotope dependent shift of position of the minimum anticipated by the BCS data is shown to be an illusion by the supplemental data.

B. The Optical Potential

The optical potential used in the analysis of the data in this thesis is the MSU potential[3,17,18]. It is displayed below :

$$2\omega U_{opt} = -4\pi\Big[\, p_1 b(r) + p_2 B(r) - \vec{\nabla}\cdot\frac{L(r)}{1+\frac{4}{3}\pi\lambda L(r)}\vec{\nabla} + \tfrac{1}{2}(1-p_1^{-1})\nabla^2 c(r) + \tfrac{1}{2}(1-p_2^{-1})\nabla^2 C(r)\,\Big]$$

with

$$b(r) = b_0\rho(r) - \varepsilon_{pi} b_1 \delta\rho \qquad c(r) = c_0\rho(r) - \varepsilon_{pi} c_1 \delta\rho$$

$$B(r) = B_0\rho^2(r) - \varepsilon_{pi} B_1 \rho\delta\rho \qquad C(r) = C_0\rho^2(r) - \varepsilon_{pi} C_1 \rho\delta\rho$$

$$L(r) = p_1^{-1} c(r) + p_2^{-1} C(r)$$

where p_1 and p_2 are the kinematic factors $p_1 = (1+\varepsilon)/(1+\varepsilon/A)$ and $p_2 = (1+\varepsilon/2)/(1+\varepsilon/2a)$. ω is the pion total energy, ε_{pi} its charge and m its mass. ε

is ω/m. $\delta\rho = \rho_p - \rho_n$ where ρ_p and ρ_n are the proton and neutron matter densities normalized to Z and A–Z, respectively. All of the isospin dependence contained in the potential appears in terms with $\delta\rho$. $\rho(r)$ is the nucleon density normalized to A. The term $\tilde{b}_0 = b_0 - (3/2\pi)(b_0^2 + 2b_1^2)k_F$ with k_F = the Fermi momentum, is the effective s–wave scattering length in the nucleus. It comes about when the the Fermi motion of the target nucleons is included in the derivation of the potential. b_0, b_1, c_0 and c_1 are the complex s–wave and p–wave single particle parameters. Isoscalar and isovector terms are distinguished by the subscripts zero and one, respectively. The single particle parameters are the coefficients in the (πN) scattering amplitude :

$$f_{pi-N} = b_0 + b_1\vec{t}\cdot\vec{\tau} + (c_0 + c_1\vec{t}\cdot\vec{\tau})\vec{k}\cdot\vec{k}'$$

Where $\vec{t}$ and $\vec{\tau}$ are the π and nucleon isospin operators, $\vec{k}$ and $\vec{k}'$ are the incoming and outgoing π momentum. These coefficients are related to the s–wave scattering lengths a_{2T}, and the p–wave scattering volumes $a_{2t,2J}$ (T the total isospin, J the total spin of the (πN) system by the following :

$$b_0 = (a_1 + 2a_3)/3 \qquad b_1 = (a_1 - a_3)/3$$

$$c_0 = (a_{11} + 2a_{13} + 2a_{31} + 4a_{33})/3$$

$$c_1 = (a_{11} - a_{13} - a_{31} + a_{33})/3$$

True absorption of the pion is described by the terms in the complex parameters B_0 and C_0. B_1 and C_1, the isovector absorption parameters which multiply $\rho\delta\rho$, are assumed to be zero throughout this analysis. This has been done primarily because there are already too many free parameters in the

theory; and for large nuclei Pauli blocking makes the process negligible. Thus, all the isospin dependence of the potential rests with the terms in the single particle parameters. The absorption part of the potential is parameterized in terms of the square of the nuclear density (ρ^2, $\rho\delta\rho$) on the assumption that it is due to at least a two nucleon process. The one step absorption process is suppressed because it doesn't conserve energy and momentum.

One of the advantages of the MSU optical potential is that it separates its reactive contents into two pieces, the absorptive part and the quasi-elastic part. The absorptive part consisting of the terms ImB_0 and ImC_0 is all the reactive part which exists for pionic atoms. The quasi-elastic part consisting of Imb_0, Imb_1, Imc_0 and Imc_1 take inelastic collisions and charge exchange reactions into account . Another advantage of the form of the potential is that it is parametrized seperately in the neutron and proton matter densities. This allows for the possible direct determination of the neutron matter radius from scattering data once the other parameters are known well enough.

The most important shortcoming of the MSU potential is the correlation between the single particle parameters and the absorption parameters. This comes about because of the fact that the square of any reasonable density model such as the square well or Fermi distribution is basically another square well or Fermi distribution times some scaling factor. Terms like $b_0\rho+B_0\rho^2$ begin to look like $(b_0+B_0\rho_{const})\rho = (b_0+B_{0Effective})\rho$. The same is true of the p-wave terms. This indicates that fits to the data cannot determine all of the parameters listed in the potential. Independent means must be used to determine some of the parameters.

The MSU potential is only semi-phenomenological in that only a few of its parameters need to be found by fitting to data. The parameter set chosen for the analysis of the data in this thesis is a modified version of what [18] calls parameter set E. As described in the reference, b_0, λ and ImB_0/ImC_0 were found by fitting to pionic atom level shifts and widths; b_1, c_1 and c_0 were taken from published (πN) phase shifts; ReB_0 and ReC_0 were arrived at by theoretical calculation [19]. ImB_0 and ImC_0 were found by fitting to 50 MeV scattering data with the ratio, ImB_0/ImC_0 fixed at its pionic atom value. This made them about 60% of their pionic atom values. The potential with these parameters was known as the compromise potential in that it did a fair job of explaining pionic atom data and elastic scattering data up to 50 MeV. (Other parameter sets did better at describing either pionic atom data or scattering data but were unable to adequately describe both simultaneously.) Since part of the data taken for this thesis was at 65 MeV parameter set E had to be modified somewhat. In particular, all the single particle parameters were obtained from phase shifts instead of only b_1, c_1 and c_0. In addition, the potential itself was slightly altered. The absorptive p-wave term was taken outside of I(r) as was done for the scattering potential in [3]. Thus $L/[1+4\pi\lambda L/3]$ was changed to $L/[1+4\pi\lambda L/3] + p_2^{-1}C(r)$ with L becoming just $p_2^{-1}c(r)$. This change is made for higher energy scattering for purely utilitarian reasons. It is known that the approach to resonance energies is accompanied by an increasing p-wave strength and the compromise form of the potential cannot accommodate this without requiring very large changes in the parameter C_0. Putting the parameter

outside the L(r) term gives C_0 more leverage and allows it to stay closer to its pionic atom value as the energy is increased. The analysis done on the 50 MeV data utilized the compromise form of the potential as given at the beginning of this section. That is, the p-wave absorption parameter remained inside the factor L(r). Also, the 50 MeV analysis used the unmodified parameters from set E.

The charge and matter density model which was used throughout the analysis was the three dimensional Fermi (wine bottle) distribution.

$$\rho(r) = \rho_0(1+\frac{wr^2}{c^2})\cdot(1+\exp[(r-c)/z])^{-1}$$

Where w is a measure of the non-constancy of the internal density, c is the origin to half-density distance, and z is the "skin thickness" or the radial separation between the 90% density point and the point at which the density has fallen to 10% of its value at the origin. ρ_0 is a normalization constant which was determined by requiring that the integral of the density distribution be equal to either the total mass or charge of the nucleus. The parameters w, c and z were obtained from electron scattering data [20]. The value of c had to be modified for the matter distribution because of the finite proton size. Thus :

$$c_{matter} = (c_{charge}^{\ 2} - c_{proton}^{\ 2})^{1/2}$$

Where c_{proton} = 0.64 fm. ρ_n and ρ_p have the same form as $\rho(r)$ but with $c=A_n$ and $c=A_p$. A_n and A_p are the neutron matter radius and proton matter radius, respectively.

The elastic cross sections were calculated from a modified Klein-Gordon equation. The Klein-Gordon equation in the absence of a potential is given by :

$$E^2 - p^2c^2 = m_0{}^2c^4$$

Where E is the total energy, m_0 is the pion rest mass and p is the quantum mechanical momentum operator. One may include the electromagnetic vector and scalar potentials $\vec{A}(r)$ and Φ by recognizing that they transform like $\vec{p}$ and E under a Lorentz transformation. Thus the Klein–Gordon equation becomes :

$$(E - e\Phi)^2 - (\vec{p} - e\vec{A}/c)^2c^2 = m_0{}^2c^4$$

Since the E–M interaction between pions and a nucleus is almost completely electrostatic the coulomb potential is taken to be $V_c = -e\Phi$. ie. $\vec{A}(r)$ is set to zero.

Because the pion nucleus interaction is not completely understood with respect to its Lorentz transformation properties, it has been commonly assumed that it can be included with the energy E and the coulomb potential V_c [21]. Thus, $E \rightarrow E - V_c - V_N$ and E^2 is approximated as $(E - V_c)^2 - 2EV_n$. Here, the terms $V_N{}^2$ and $2V_cV_N$ are arbitrarily dropped from the E^2 term.

The modified Klein–Gordon equation was numerically integrated for each partial wave starting at the origin and proceeding out to a matching point at 24 fm. At the matching point the logarithmic derivative of the resulting wave–function was compared to that of the wave function which was found as the solution to the coulomb scattering problem in the absence of a nuclear potential. The complex phase shifts obtained in the process were then utilized to calculate the scattering amplitude and finally the differential cross section.

C. Theoretical Predictions and Fits to the Data

The MSU potential was used to predict the 65 MeV differential cross sections. The single particle parameters were taken from scattering lengths and volumes which were calculated from published pi–nucleon phase shifts [16]. These parameters were found to exptrapolate smoothly to the corresponding "parameter set E" values at 50 MeV. The absorption parameters were taken from "parameter set E". The Neutron matter radius was taken to be the same as the proton matter radius.

The π^+ calculation agreed well with the data except at some forward angle points (See Fig. IV–5). It successfully predicted the deep and narrow first minima and the virtual lack of isospin dependence. The π^- prediction is a different story. The predicted values of the differential cross sections differed noticeably from the data at all but the most forward angles (See Fig. IV–6). The predicted first minimum was very shallow and occured at a much lower scattering angle. The data and the calculation agreed on the fact that a noticeable isospin difference dependence emerged for angles past the minimum and they agreed on the relative ordering of the dependence. This agreement implies that the single particle part of the MSU potential is doing its job since it is the single particle terms which contain all the isospin dependence.

MSU predictions were also made for the 50 MeV data. As was already mentioned, the compromise form of the MSU potential with parameters from parameter set E was used for the 50 MeV analysis. For the purpose of comparison with the 65 MeV results, which involved both π^+ and π^- cross

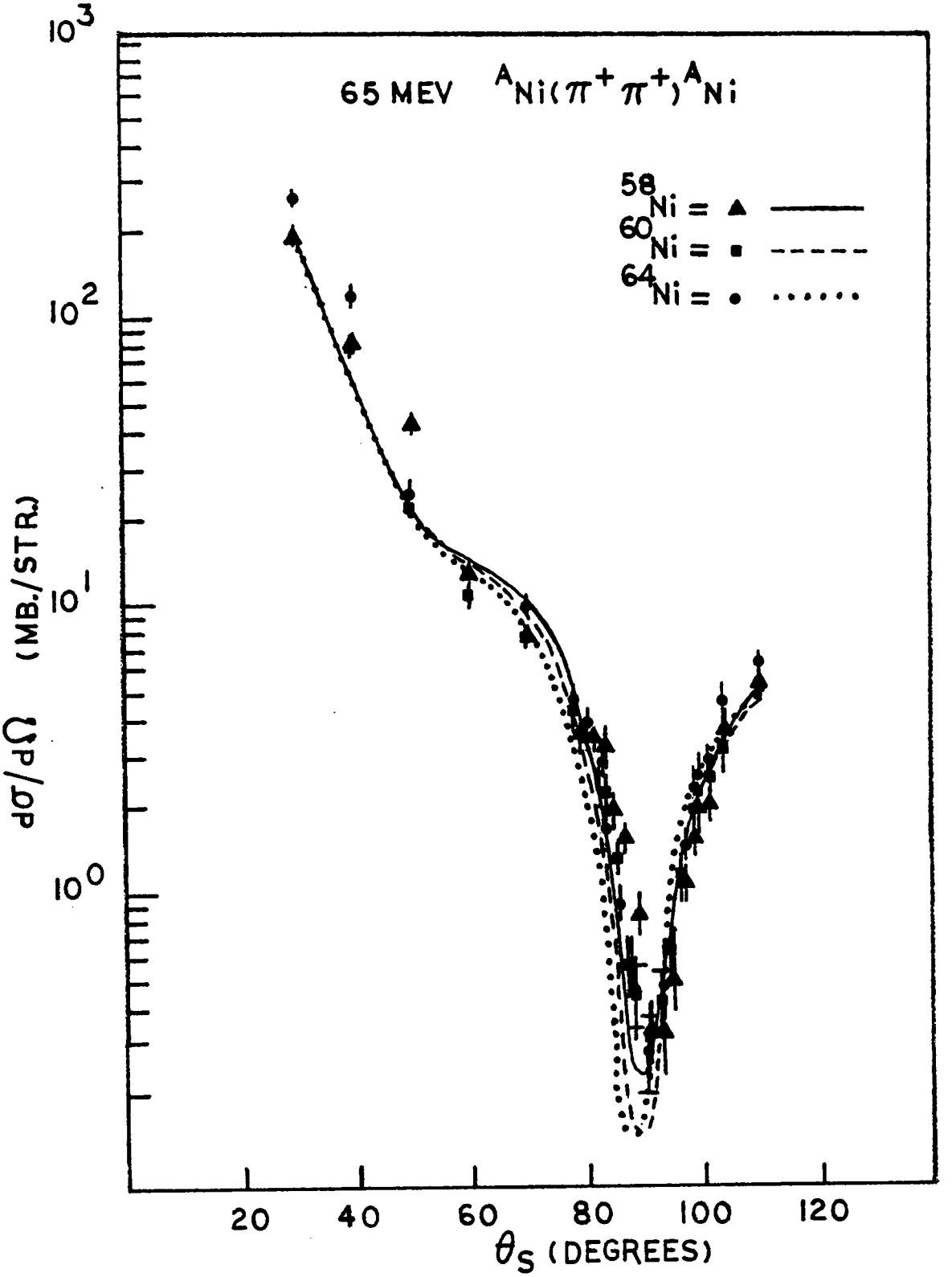

Figure IV-5 MSU predictions for 65 MeV pi+ scattering.

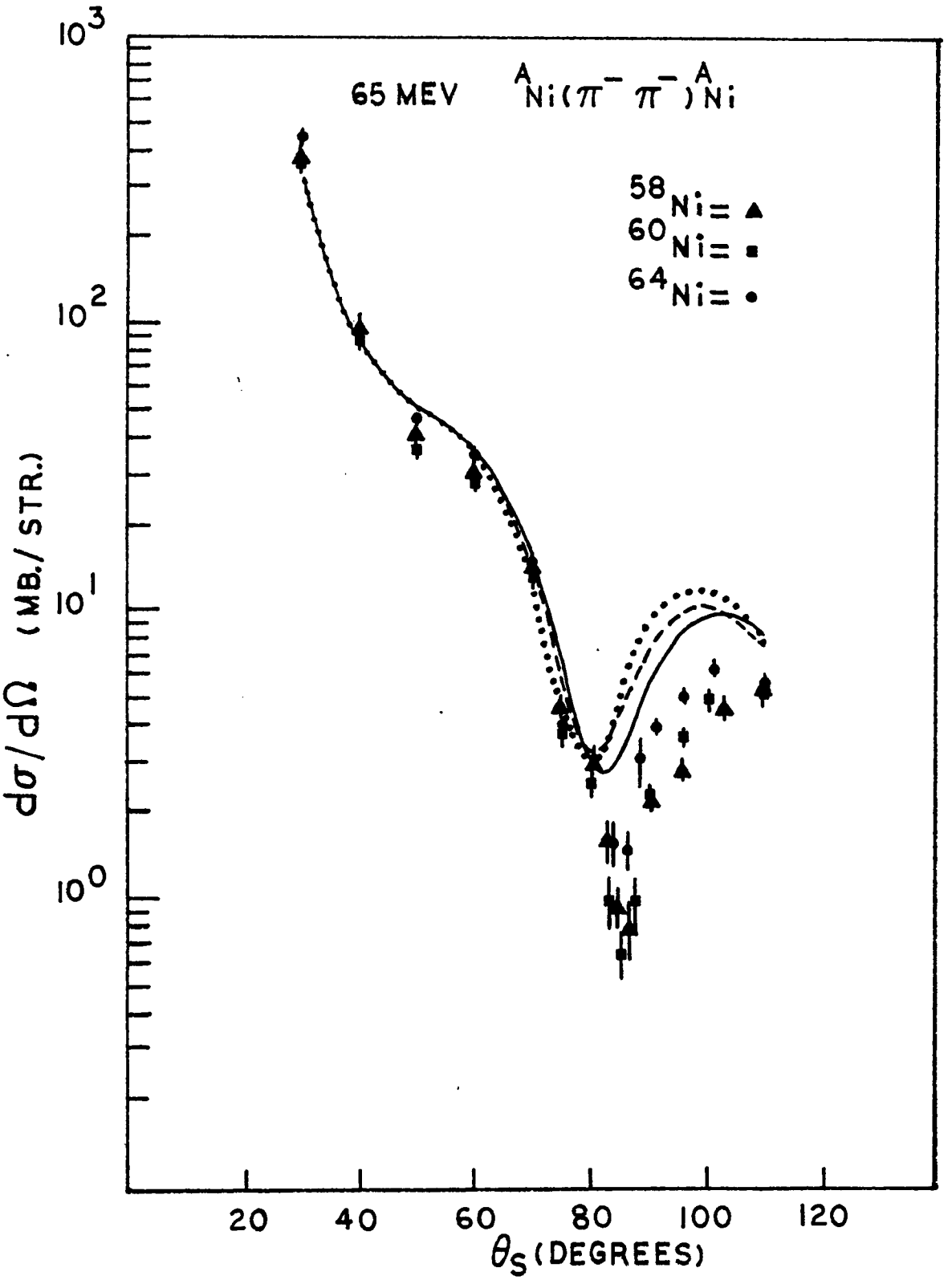

Figure IV-6 MSU predictions for 65 MeV pi- scattering.

sections, MSU predictions were made for π^+ ^{58}Ni and ^{64}Ni scattering at 50 MeV in addition to the π^- scattering. The π^+ data was take from [3]. It can be seen from figures IV–7 thru IV–10 that the π^- predictions are qualitatively similar to the data. The χ^2 are very large, at 281 for ^{58}Ni and 292 for ^{64}Ni. (χ^2 here, and in the remainder of this thesis, means χ^2 per degree of freedom) The π^+ predictions are much closer to the data. The χ^2 for both cross sections is at least an order of magnitude smaller than the corresponding π^- χ^2.

The fact that in the case of both the 50 MeV data and the 65 MeV data the MSU predictions were much better for π^+ scattering than π^- suggests that different potentials may be necessary for different pion charge. This possibility will be explored in the present analysis. The next step in the analysis was to vary the complex absorption parameters C_0 and B_0 and the neutron matter radius A_n in order to try to more closely mirror the 65 MeV data. Unfortunately, ReC_0 and A_n are highly correlated as can be ascertained by noting the magnitude of the off–diagonal error matrix elements when obtaining a fit with all of the above left to vary simultaneously. Thus, only the absorption parameters were allowed to vary and A_n was kept fixed at the proton matter radius. In addition, the ratio ImB_0/ImC_0 was kept constant at its value determined by fits to pionic atom data.

As can be seen in figures IV–11 and IV–12 there is no great improvement in the agreement between data and prediction for the π^+ data. However, there is a tremendous improvement for the π^- data. This implies that

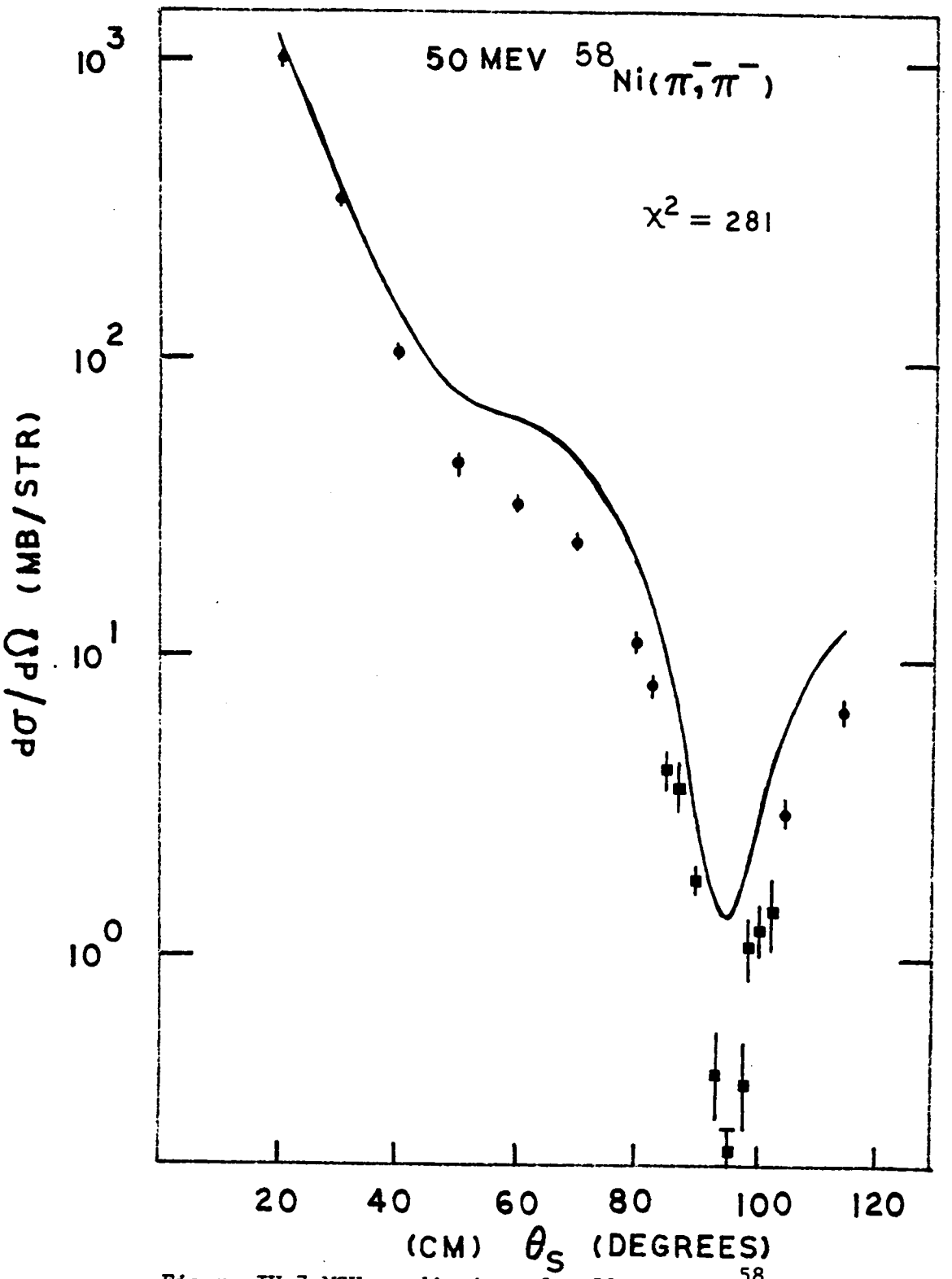

Figure IV-7 MSU predictions for 50 MeV pi- ^{58}Ni scattering.

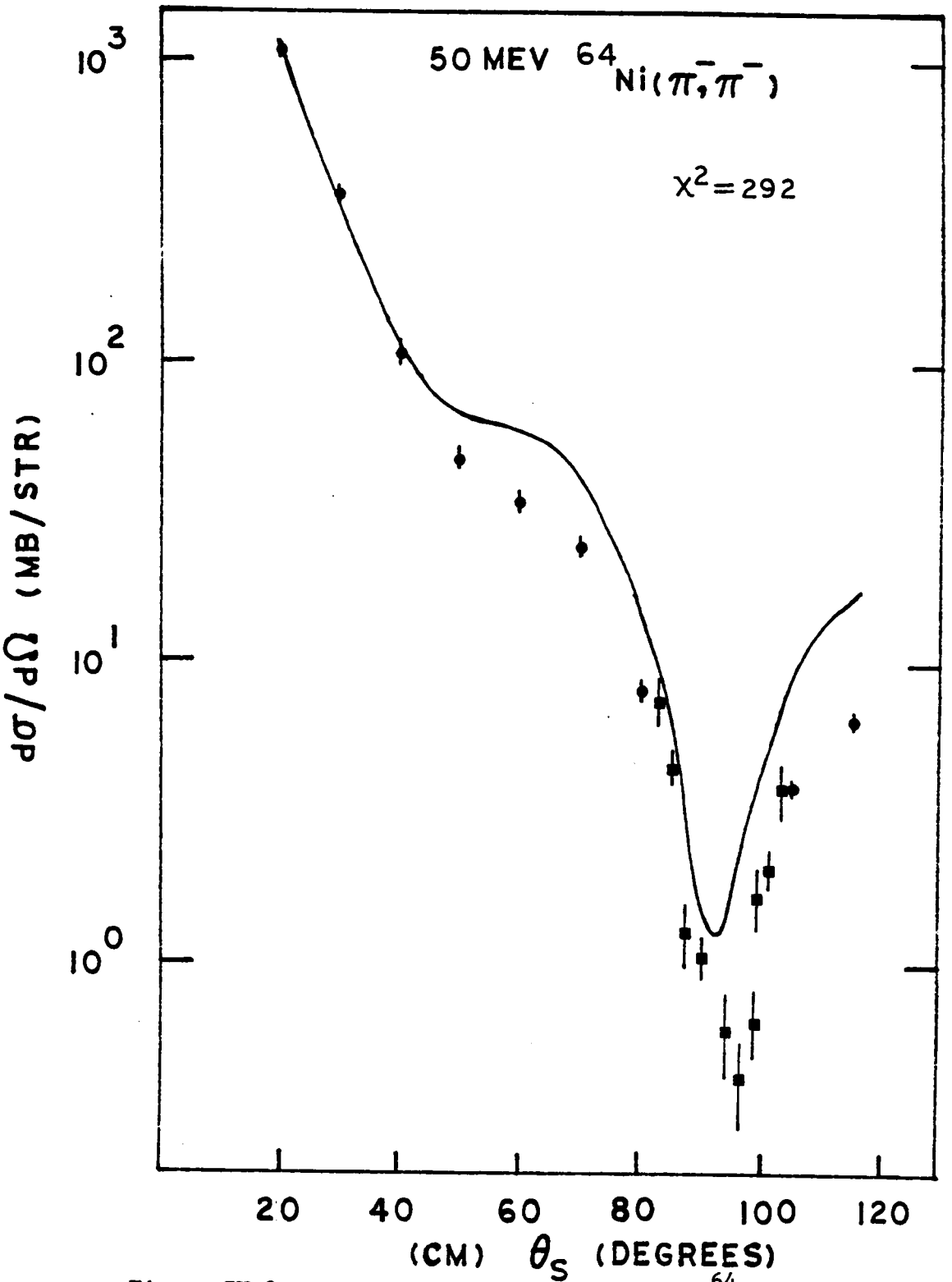

Figure IV-8 MSU predictions for 50 MeV pi- ^{64}Ni scattering.

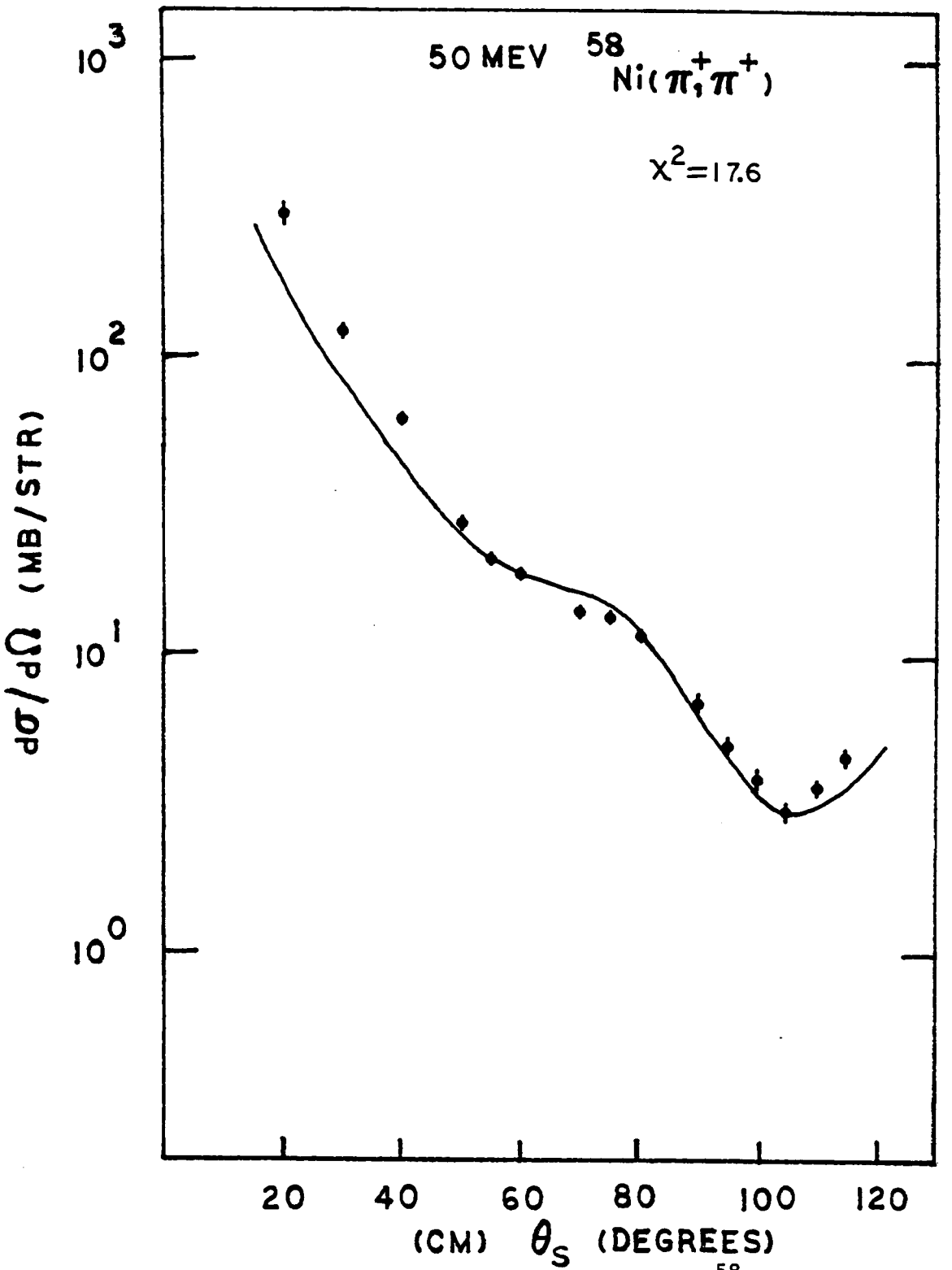

Figure IV-9 MSU predictions for 50 MeV pi+ ^{58}Ni scattering.

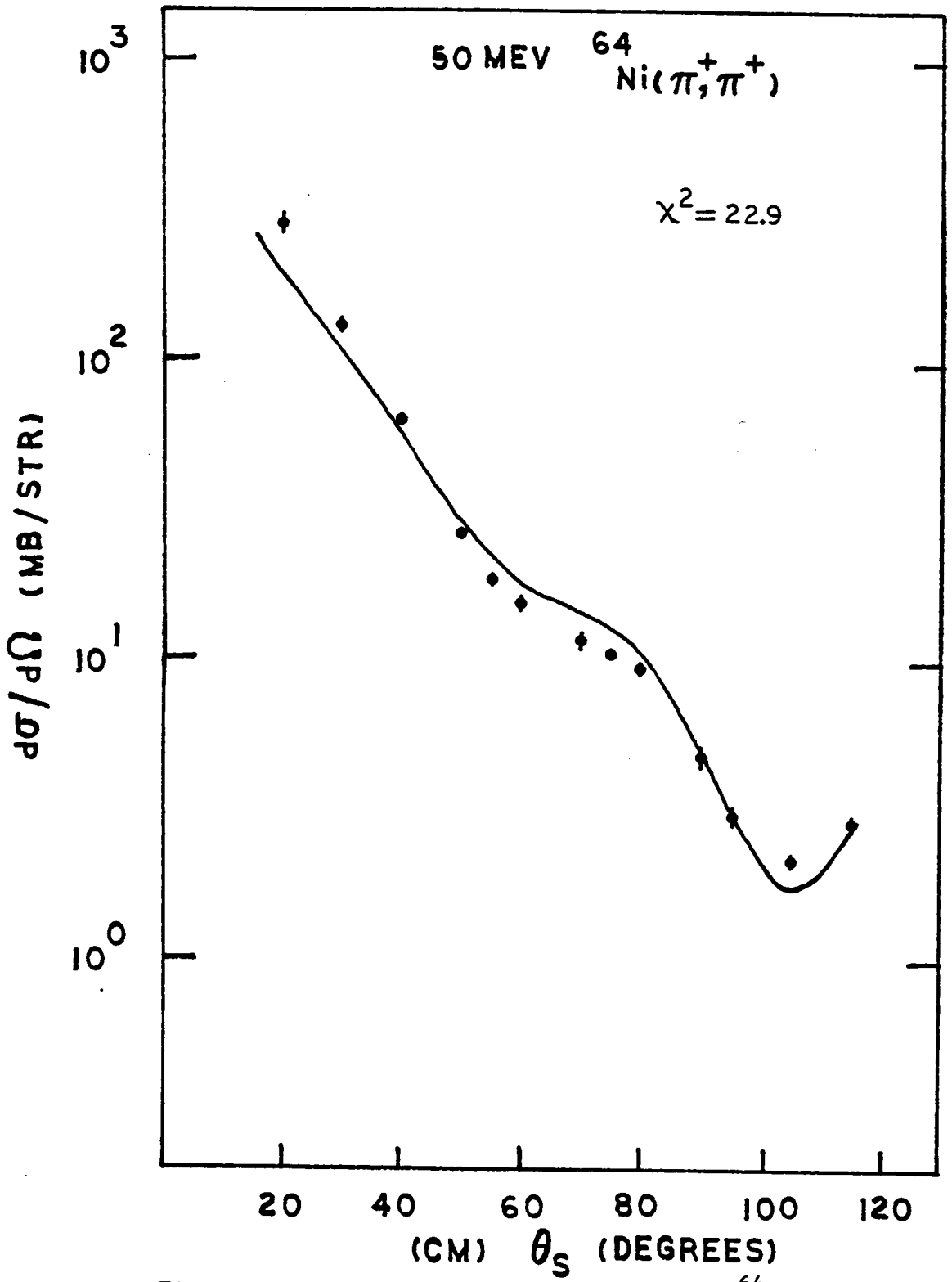

Figure IV-10 MSU prediction for 50 MeV pi+ ^{64}Ni scattering.

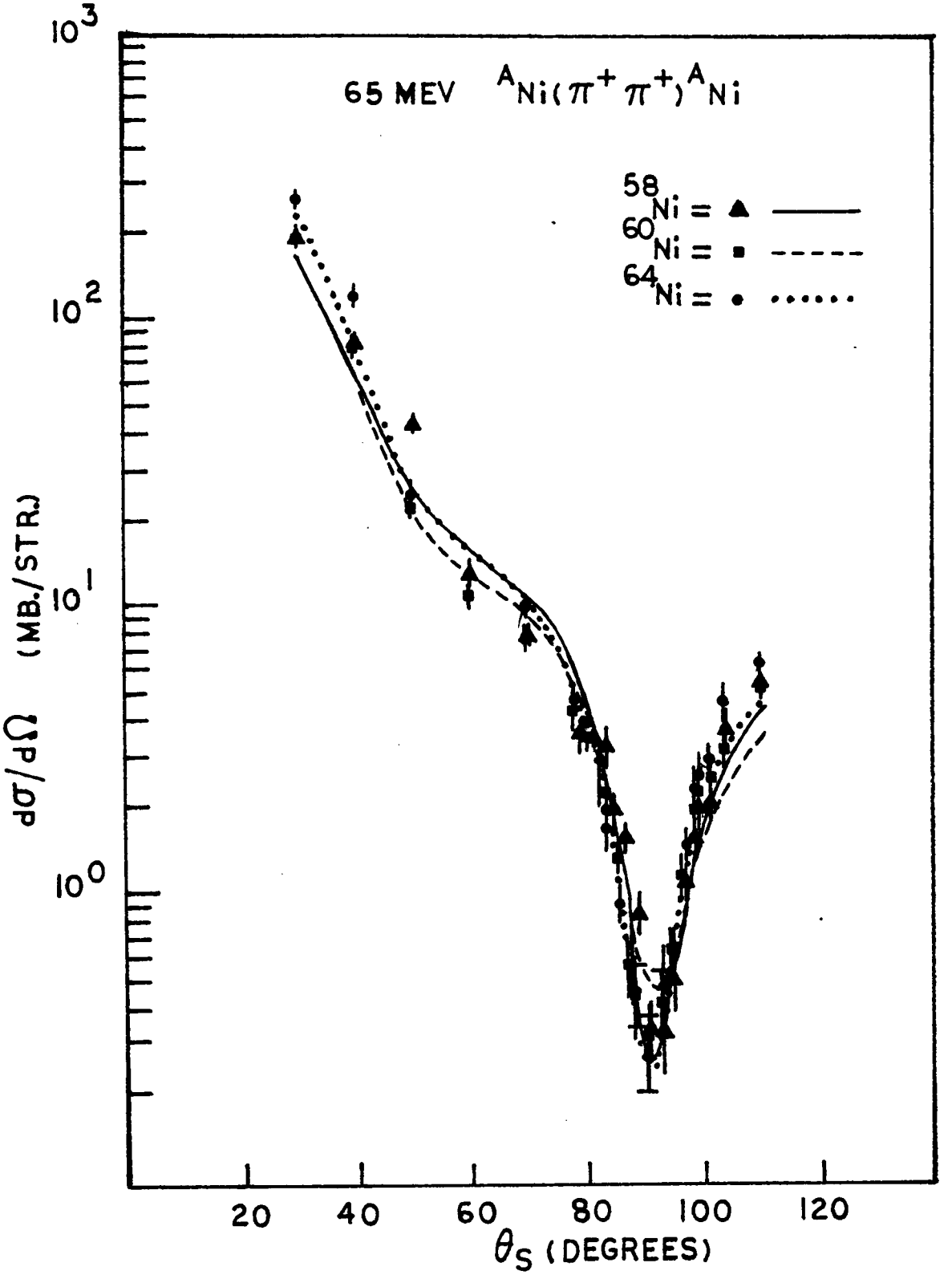

Figure IV-11 MSU fit to 65 MeV pi+ data, varying absorp. params.

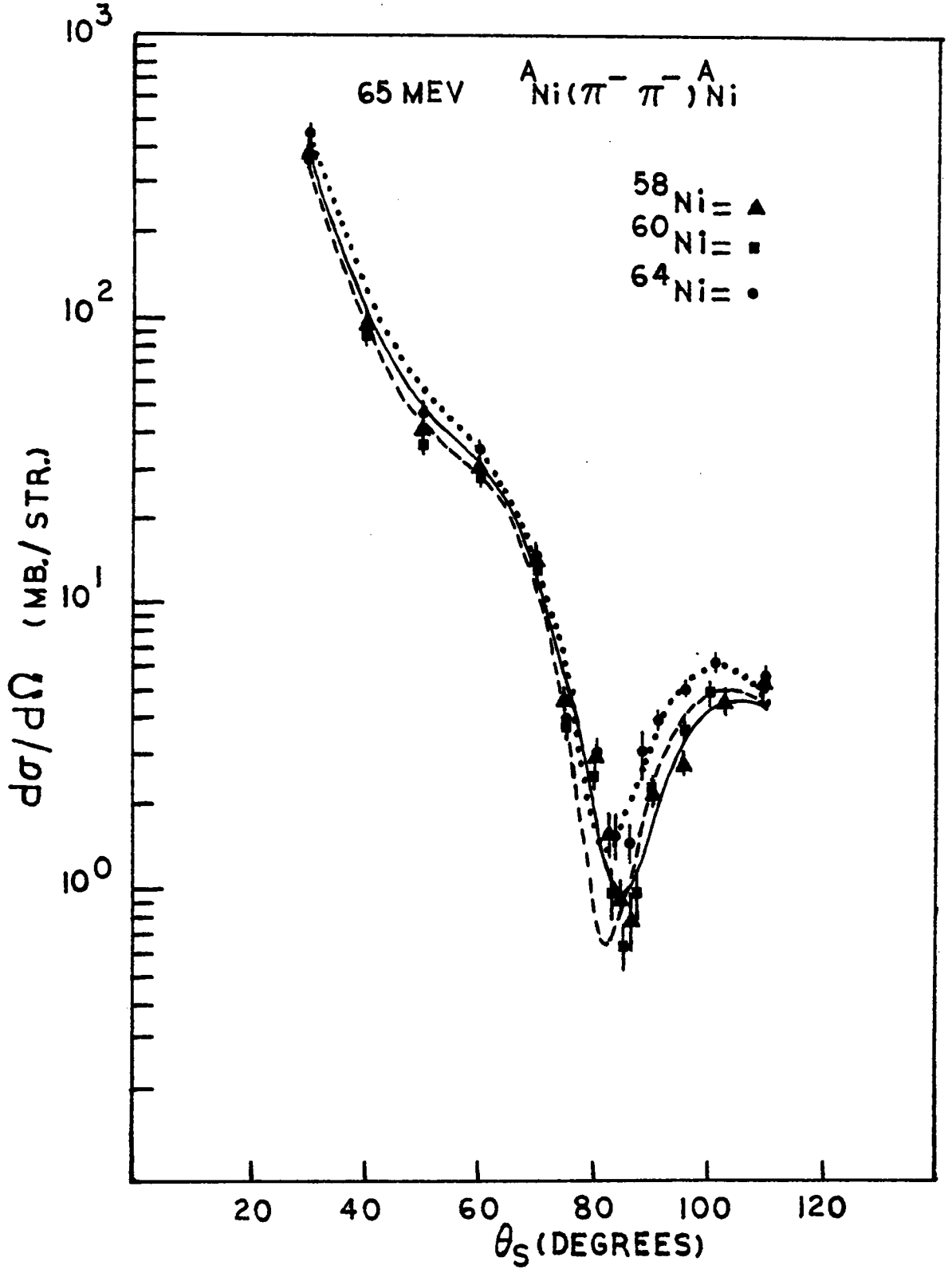

Figure IV-12 MSU fit to 65 MeV pi- data, varying absorp. params.

perhaps the true absorption part of the MSU potential is different for π^+ and π^-. In order to explore this further the values of the absorption parameters determined in the fits were plotted versus target isotope and pion charge in figures IV–13 and IV–14. Only ReB_0, ReC_0 and ImC_0 are plotted because of the fixed ratio between the imaginary parameters. The only parameter which is well determined is ReC_0. It should be noted that ReC_0, though well determined takes on two different values, one for π^+ and one for π^-. The rest of the absorption parameters show no such dependence.

A similar process was performed on the 50 MeV data. The results of the fits are given in figure IV–15 and IV–16. The determined values for the absorption parameters are plotted in figure IV–17. The same situation of a well defined ReC_0 with two different values for π^+ and π^- is encountered.

Because of the correlation between A_n and ReC_0 mentioned above, there exists the possibility that the neutron matter radius which was left fixed could produce the same result if varied. Thus, in an attempt to reconcile the apparently different potentials for π^+ and π^-, the next step was to try to fit the π^- data for both 50 MeV and 65 MeV by varying A_n and leaving the absorption parameters fixed at their π^+ values. The absorption parameters were set at those values because it was found that the π^+ cross section is insensitive to variation in A_n. The results were conclusive. At both energies the neutron matter radius was unable to mimic the effects of simply varying the absorption parameters. In the case of ^{58}Ni at 65 MeV the χ^2 of the A_n fit was

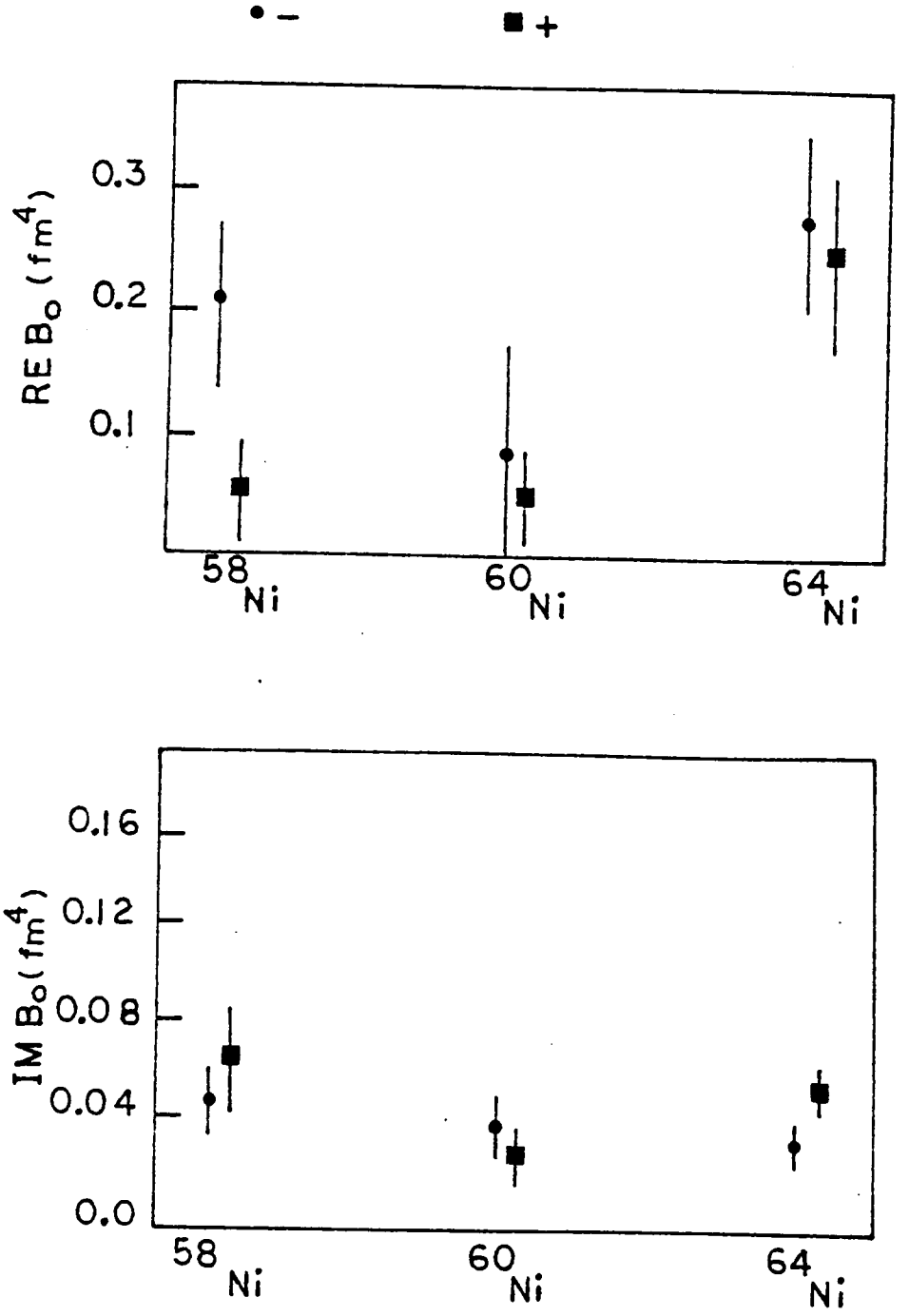

Figure IV-13 Absorption parameters ReB_0 and ImB_0, determined from MSU fit to 65 MeV pi^+ and pi^- data.

Q_π	A	χ^2
+	58	9.4
+	60	5.6
+	64	6.3

Q_π	A	χ^2
−	58	10.5
−	60	8.1
−	64	10.7

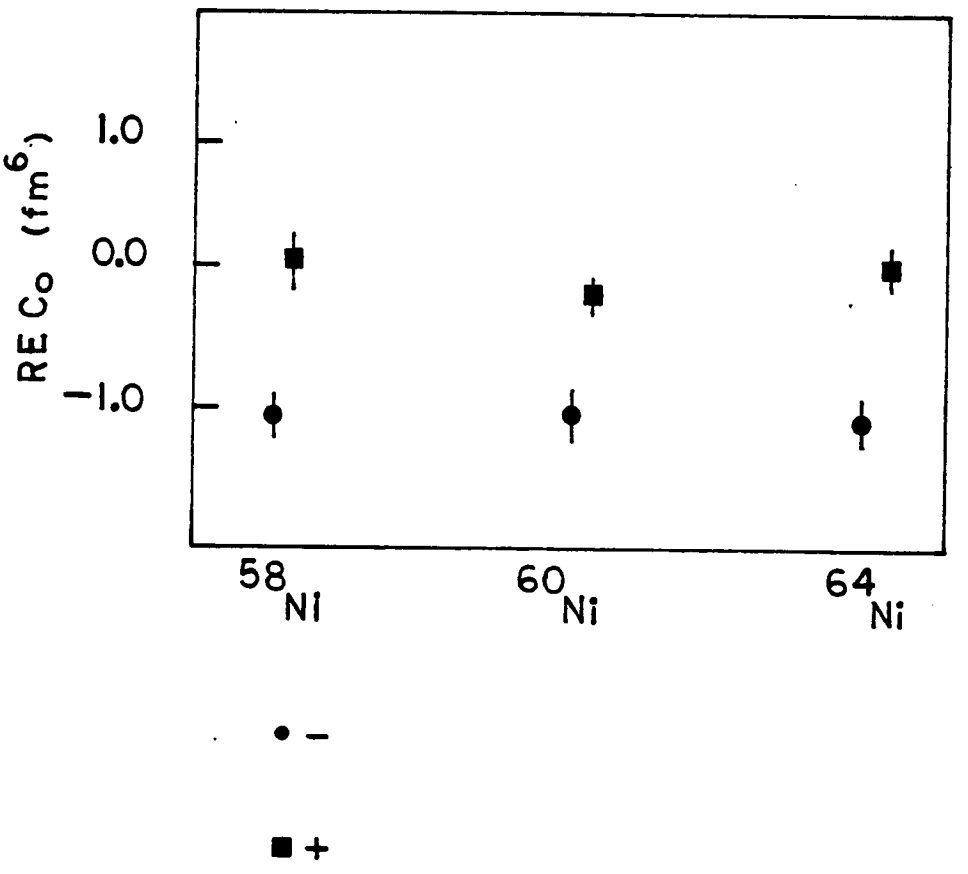

Figure IV-14 Absorption parameter ReC_0, determined from MSU fit to 65 MeV pi+ and pi- data.

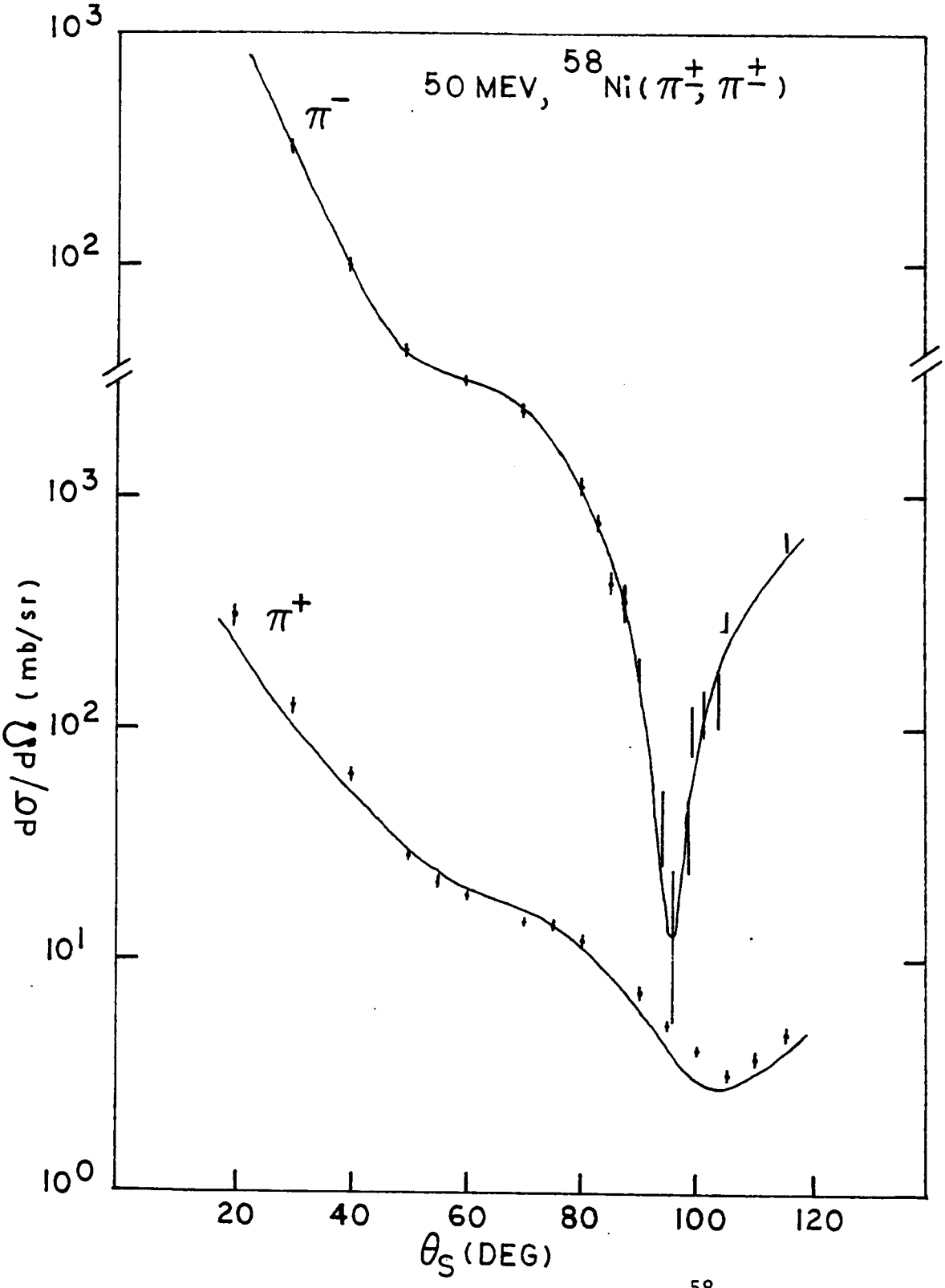

Figure IV-15 MSU fit to 50 MeV pi+ and pi- ^{58}Ni data, varying the absorption parameters.

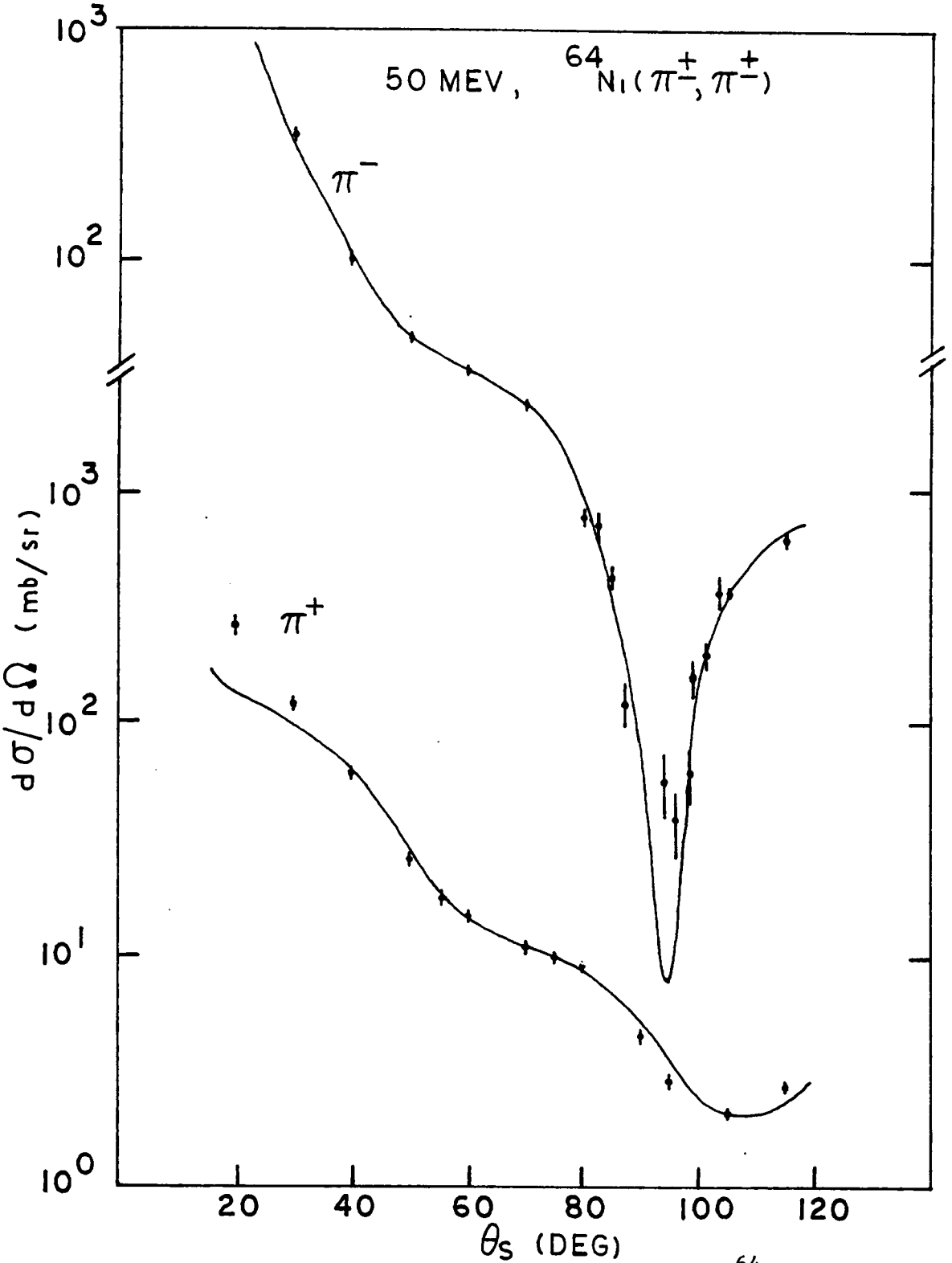

Figure IV-16 MSU fit to 50 MeV pi+ and pi- ^{64}Ni data, varying the absorption parameters.

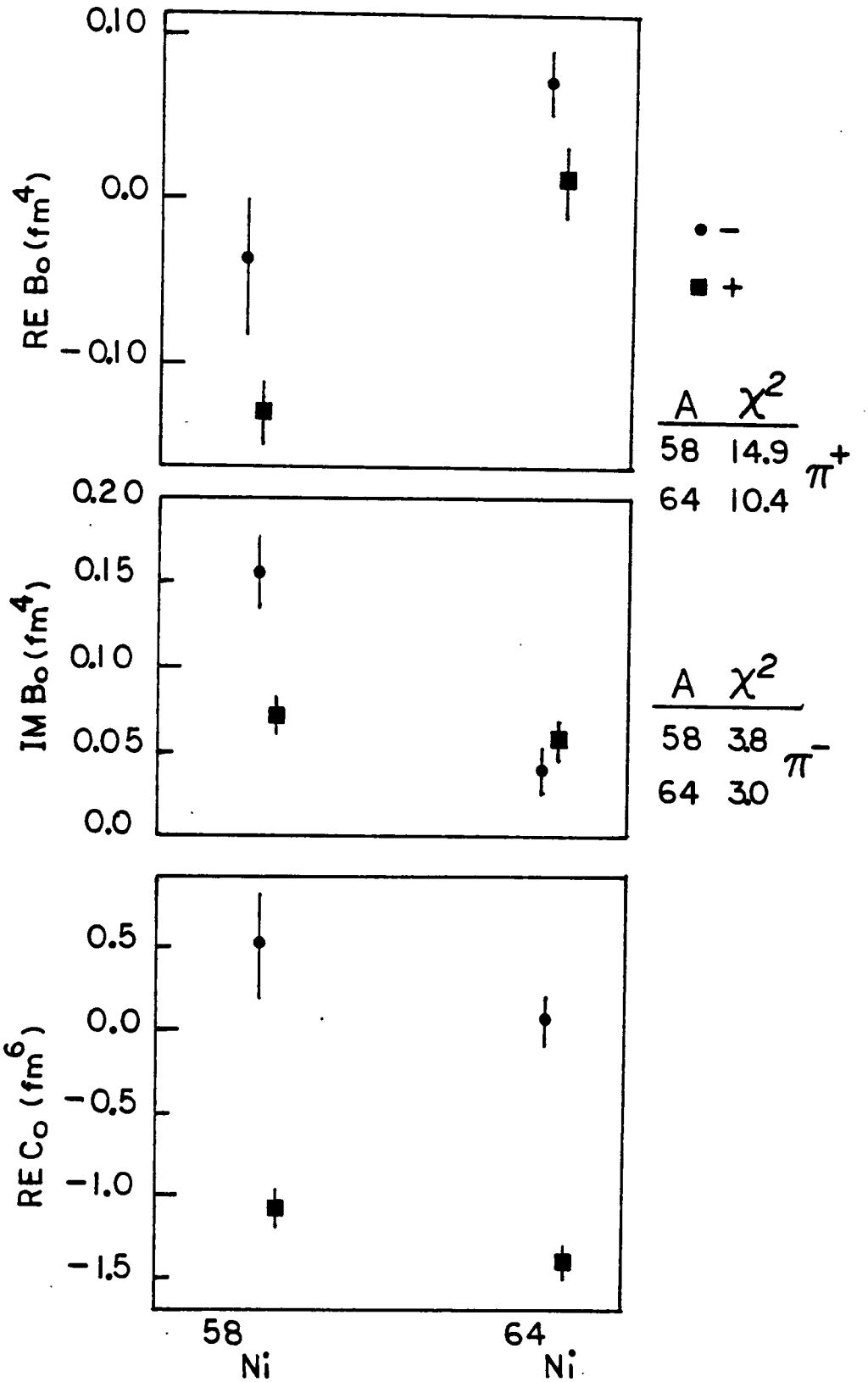

Figure IV-17 Absorp. params. ReB_0, ImB_0 and ReC_0 determined from MSU fit to 50 MeV pi+ and pi- data.

an order of magnitude larger than the absorption parameter fit. For the other isotopes it was worse. The resulting neutron matter radii obtained in these fits were between 0.5 and 1.0 fermi smaller than the corresponding proton matter radii, which is preposterous. At 50 MeV, the best χ^2 for ^{58}Ni was 600. For ^{64}Ni it was 87. The χ^2 obtained for these when varying the absorption parameters was only 3.8 and 3.0, respectively. The changes in the neutron matter radii which were required above were +0.1 fermi for ^{58}Ni and +0.3 fermi for ^{64}Ni. Thus, the data indicates that at least the absorption part of the MSU potential differs in accordance with the charge of the pion.

Chapter V

Summary

Experiment 814 was an opportunity to "shake down" the total Clamshell spectrometer system of magnet, wire chambers, electronics, software etc. As this thesis reveals, no major problems were encountered. The spectrometer successfully obtained elastic scattering data at 50 MeV and 65 MeV with a best energy resolution of 600 KeV. Confidence was found for both the spectrometer system and the data reduction process from the fact that the 50 MeV π^- data for ^{58}Ni and ^{64}Ni targets joined smoothly with the data taken using the Bicentennial Spectrometer. In addition, the new 50 MeV data was better able to define the characteristics of the first minimum.

The 65 MeV elastic data was compared to preditions made by the MSU optical potential. The predictions and the π^- data were not found to be in agreement with each other but it was possible to obtain good agreement by varying the absorption parameters C_0 and B_0. The real part of the p-wave absorption parameter was well determined in this process but had two different values depending on whether the fit was to π^+ or π^- data. The results of a similar analysis performed on the 50 MeV data, using the compromise form of the MSU potential along with parameters from set E, reaffirm this finding. Since the effect could not be adequately reproduced by varying the neutron matter radius A_n one must conclude that either the potential in its present form

requires two different sets of absorption parameters at higher energies for π^+ and π^- or the present form of the absorptive part of the MSU potential is inadequate.

References

1. N. C. Francis and K. M. Watson, Physical Review 92, 291 (1953)

2. M. Ericson and T. E. O. Ericson, Annals of Physics 36, 323 (1966)

3. K. Stricker, H. McMannus and J. A. Carr, Physical Review C 19, Number 3, 929 (1979)

4. S. Mishra et al. (to be published)

5. R. L. Burman et al., Nuclear Instruments and Methods 131, 29 (1975)

6. LAMPF Users Handbook (Los Alamos, New Mexico : Los Alamos Meson Physics Facility, Oct. 1984) Number MP-D0-3-UHB

7. L. V. Coulson et al., Nuclear Instruments and Methods 101, 247 (1972)

8. E. A. Wadington et al., Nuclear Instruments and Methods 134, 243 (1976)

9. S. Kowalski and H. Enge (to be published)

10. L. G. Atencio et al., Nuclear Instruments and Methods 187, Numbers 2,3 243 (1981)

11. S. Shlaer, An MBD Primer (Los Alomos, Mew Mexico : Los Alamos Scientific Laboratory, Aug. 1974) Number LA-5511-MS

12. Group MP-1, Introduction to Q (Los Alamos, New Mexico : Los Alamos Meson Physics Facility, Oct. 1982) Number MP-1-3401-3

13. R. L. Boudrie et al., IEEE Transactions on Nuclear Science, NS-26 Number 4, 4588 (Aug. 1979)

14. Group MP-1, Users Information Manual, A Data Testing Package Under RSX-11 (Los Alamos, New Mexico : Los Alamos Meson Physics Facility, Oct. 1982) Number MP-1-3412-3

15. Group MP-1, Users Information Manual, A Histogramming System Under RSX-11M (Los Alamos, New Mexico : Los Alamos Meson Physics Facility, Oct. 1982) Number MP-1-34007-4

16. R. A. Arndt and L. D. Roper, Centre for Analysis of Particle Scattering, Internal Report CAPS–80–3, 1982

17. K. Stricker, H. McMannus and J. A. Carr, Physical Review C 22, Number 5, 2043 (1980)

18. J. A. Carr et al., Physical Review C 25, Number 2, 952 (1981)

19. D. Chai and D.O. Riska, Nuclear Physics A329, 429 (1979)

20. C. W. DeJager et al., Atomic Data and Nuclear Data Tables, 14, 479 (1974)

21. R. A. Eisenstein and G. A. Miller, Computer Physics Communications 8, 130 (1974)

Appendix A

Finite Solid Angle and Beam Spot Size Corrections

The differential cross section for a hypothetical point target spot which is displaced slightly from the center of the real target spot and a hypothetical point spectrometer aperature also displaced slightly from the real aperature's center can be expanded in the following manner:

$$\sigma(\Theta+\beta) = \sigma(\cos(\Theta)) + \sigma'(\cos(\Theta))\cdot[\cos(\Theta+\beta)-\cos(\Theta)]$$

$$+\sigma''(\cos(\Theta))\cdot[\cos(\Theta+\beta)-\cos(\Theta)]^2/2 + \ldots$$

where Θ is the central scattering angle and $\Theta+\beta$ is the scattering angle of the trajectory defined by the vector $\vec{R}$. $\vec{R}$ is the vector between the hypothetical point target spot and point aperature, $\vec{R}_0$ is the vector between the real target spot center and aperature center. From figure A-1 the vector $\vec{R}$ has components along the axes x_0, y_0, z_0 as follow:

$$\vec{R} = [\ x-u\ ,\ R_0\sin(\Theta) + y\cos(\Theta) - v\cos(\vartheta_t)\ ,\ R_0\cos(\Theta) - y\sin(\Theta) + v\sin(\Theta_t)\ ]$$

The measured cross section can be found by integrating the expansion for $\sigma(\Theta+\beta)$ over the solid angle and the target spot. Thus :

$$\sigma_m(\Theta+\beta) = \sigma(\cos(\Theta)) + \frac{\sigma'(\cos(\Theta))\cdot\int\int[\cos(\Theta+\beta)-\cos(\Theta)]d\Omega d\chi}{\int\int d\Omega d\chi}$$

$$+ \frac{\sigma''(\cos(\Theta))\cdot\int\int[\cos(\Theta+\beta)-\cos(\Theta)]d\Omega d\chi}{2\int\int d\Omega d\chi} + \ldots$$

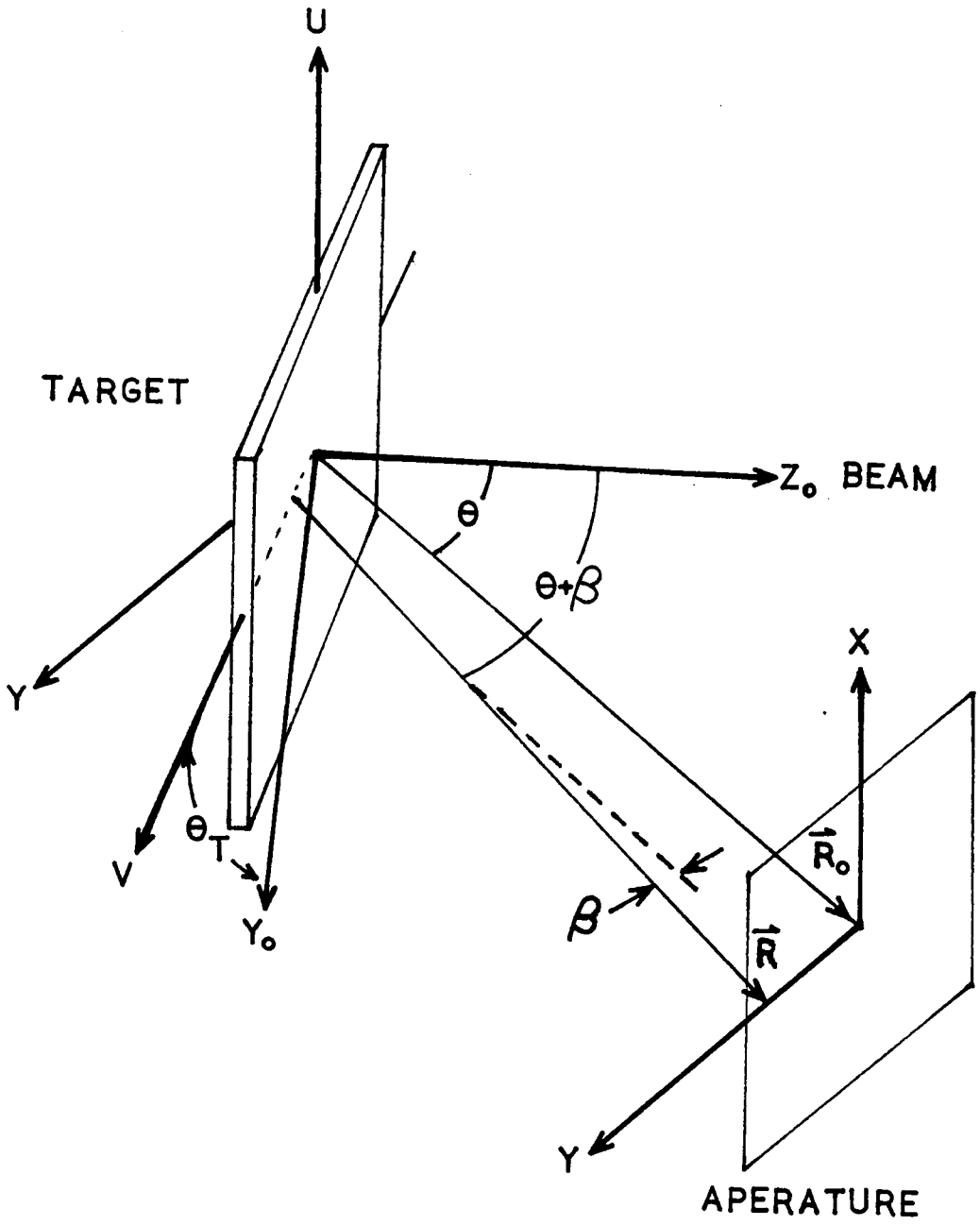

Figure A-1 Finite solid angle and beam spot geometry used in correction calculation.

One can re-express $\cos(\Theta+\beta)$ in terms of x, y, u, v, Θ, Θ_t and R_0 as follows :

$$\cos(\Theta+\beta) = \left[\frac{\cos(\Theta) - b\sin(\Theta) + d\sin(\Theta_t)}{(1+Q)^{1/2}} \right]$$

where

$$Q = a^2+b^2 + c^2 + d^2 - 2ac - 2bdcos(\Theta-\Theta_t) - 2dsin(\Theta-\Theta_t)$$

and $a = x/R_0$, $b = y/R_0$, $c = u/R_0$ and $d = v/R_0$

similarly, $d\Omega d\chi = \frac{\hat{R}\cdot\hat{R}_0}{R^2}\, dxdydudv$

$$= \frac{R_0^2[1-d\sin(\Theta-\Theta_t)]}{(1+Q)^{3/2}}\, dadbdcdd$$

The definite integrals are then performed between the limits $\pm\Delta_X$, $\pm\Delta_Y$, $\pm\Delta_U$ and $\pm\Delta_V$ where these quantities were already defined in section F of chapter III.

For the binned cross sections the data was collected according to user defined angular ranges and not according to the geometry of the target or spectrometer aperature. Thus, the step above, in which $\cos(\Theta+\beta)$ was re-cast in terms of the target coordinates and aperature coordinates, is not needed since the limits on the angular deviation, β, is given at the start. In this case a cross section measurement yields $\int\sigma d\Omega/\int d\Omega$ with $d\Omega = d\cos(\Theta)d\Phi$. Let $\sigma(\cos(\Theta) = F(x)$ then one can write:

$$F(x) = F(x_0) + F'\cdot(x-x_0) + F''\cdot(x-x_0)^2/2 + \ldots$$

The measured F(x) is then obtained by integrating with respect to x over the bin limits :

$$F(x)_m = F(x_0) + F'\cdot\left[\frac{\int x\,dx}{\int dx} - x_0\right] + F''\cdot\left[\frac{\int x^2\,dx}{\int dx} - 2x_0\frac{\int x\,dx}{\int dx} + x^2\right] + \ldots$$

$$= F(x_0) + F'\cdot\left[\frac{x_2^2-x_1^2}{2(x_2-x_1)} - x_0\right] + F''\cdot\left[\frac{x_2^3-x_1^3}{3(x_2-x_1)} - x_0\frac{(x_2^2-x_1^2)}{x_2-x_1} + x_0^2\right]$$

Where x_0, x_1 and x_2 are as defined in section F of chapter III. The factor of 2π which arises from the integration over Φ cancels in all of the above. It should be noted that several of the terms above whould cancel if x_0 were equal to $(x_2-x_1)/2$. However, it is the angular limits which are symmetric about a central angle Θ and not their cosines x_0, x_1 and x_2.

Appendix B

Experimental Data Tables

The data displayed in the following set of tables do not include the absolute normalization error of 6.0% and 6.8% for 65 MeV and 50 MeV. The origins of the quoted errors are described in chapter III section E.

Table B-1

65 MeV π^+ ^{58}Ni Differential Cross sections

Θ_{cm} (deg.)	σ_{cm} (mb./sr.)	$\Delta\sigma_{cm}$ (mb./sr.)
30.11	197.6	10.92
40.14	86.79	4.287
50.17	45.53	2.425
60.19	13.50	0.879
70.20	8.399	0.427
79.21	3.833	0.589
81.41	3.684	0.406
83.72	3.387	0.675
84.22	2.018	0.316
86.52	1.636	0.192
87.87	0.904	0.155
91.22	0.362	0.089
93.52	0.350	0.115
95.02	0.532	0.115
97.31	1.167	0.151
99.61	2.109	0.428
99.31	1.643	0.268
101.6	2.141	0.257
103.9	3.894	0.778
110.2	5.839	0.273

Table B–2

65 MeV π^+ ^{60}Ni Differential Cross sections

Θ_{cm} (deg.)	σ_{cm} (mb./sr.)	$\Delta\sigma_{cm}$ (mb./sr.)
40.13	81.09	4.199
50.16	22.75	1.530
60.18	10.97	0.727
70.20	8.191	0.383
78.30	4.283	0.676
80.61	3.624	0.404
82.91	2.427	0.489
83.41	2.256	0.359
85.71	1.356	0.170
87.91	0.584	0.147
88.61	0.461	0.140
90.91	0.334	0.099
93.21	0.429	0.117
94.31	0.690	0.127
96.61	1.196	0.215
98.91	1.973	0.390
99.21	2.266	0.361
101.5	2.586	0.293
103.8	3.271	0.661
110.2	5.380	0.311

Table B–3

65 MeV π^+ ^{64}Ni Differential Cross sections

Θ_{cm} (deg.)	σ_{cm} (mb./sr.)	$\Delta\sigma_{cm}$ (mb./sr.)
30.10	258.2	13.13
40.13	118.6	6.196
50.15	24.32	2.065
60.17	12.90	0.749
70.18	9.864	0.460
78.29	4.721	0.744
80.59	3.954	0.443
82.89	2.772	0.559
83.59	1.683	0.278
85.90	0.944	0.138
88.20	0.587	0.157
89.30	0.461	0.114
91.60	0.295	0.082
93.90	0.480	0.182
95.20	0.627	0.127
97.39	1.501	0.188
99.19	2.822	0.496
99.69	2.984	0.469
101.5	4.725	0.333
103.8	6.353	0.933
110.2	2.441	0.368

Table B-4

65 MeV π^- ^{58}Ni Differential Cross sections

Θ_{cm} (deg.)	σ_{cm} (mb./sr.)	$\Delta\sigma_{cm}$ (mb./sr.)
30.11	383.0	28.58
40.14	93.24	7.29
50.17	41.40	2.293
60.19	32.19	1.392
70.20	15.30	0.788
75.21	4.822	0.438
81.11	3.170	0.234
83.11	1.654	0.295
85.42	0.953	0.150
87.72	0.823	0.185
90.92	2.278	0.132
96.22	2.866	0.149
101.5	4.687	0.227
110.2	5.166	0.245

Table B-5

65 MeV π^- ^{60}Ni Differential Cross sections

Θ_{cm} (deg.)	σ_{cm} (mb./sr.)	$\Delta\sigma_{cm}$ (mb./sr.)
30.10	364.8	21.82
40.13	89.34	7.12
50.16	36.54	2.24
60.18	27.90	1.266
70.20	13.20	0.692
75.20	3.816	0.389
80.31	2.572	0.216
83.11	1.035	0.234
85.41	0.668	0.134
87.71	1.042	0.232
90.21	2.312	0.123
95.91	3.788	0.187
100.5	4.867	0.244
110.2	5.293	0.256

Table B–6

65 MeV π^- ^{64}Ni Differential Cross sections

Θ_{cm} (deg.)	σ_{cm} (mb./sr.)	$\Delta\sigma_{cm}$ (mb./sr.)
30.10	439.8	26.08
40.13	94.05	8.482
50.15	46.78	2.713
60.17	35.19	1.594
70.18	14.81	0.830
75.19	4.127	0.429
80.89	3.062	0.207
84.10	1.585	0.296
86.40	1.506	0.215
88.70	3.168	0.651
91.50	3.474	0.183
96.20	5.184	0.242
101.3	6.459	0.320
110.2	5.815	0.316

Table B–7

50 MeV π^- ^{58}Ni Differential Cross sections

Θ_{cm} (deg.)	σ_{cm} (mb./sr.)	$\Delta\sigma_{cm}$ (mb./sr.)
82.70	7.925	0.619
85.00	4.299	0.499
87.30	3.581	0.749
93.90	0.395	0.145
96.20	0.146	0.130
98.50	0.357	0.137
98.90	1.045	0.251
101.2	1.201	0.238
103.5	1.382	0.377

Table B–8

50 MeV π^- ^{64}Ni Differential Cross sections

Θ_{cm} (deg.)	σ_{cm} (mb./sr.)	$\Delta\sigma_{cm}$ (mb./sr.)
82.68	7.600	1.21
84.98	4.564	0.548
87.28	1.277	0.319
93.88	0.609	0.196
96.18	0.410	0.138
98.48	0.649	0.178
98.88	1.690	0.337
101.2	2.102	0.303
103.5	3.917	0.797

The vita has been removed from the scanned document